Developments in the Built Environment 22 (2025) 100644

Contents lists available at ScienceDirect

Developments in the Built Environment

journal homepage: www.sciencedirect.com/journal/developments-in-the-built-environment

Probabilistic prediction of Load–Displacement curves of corroded strands

Seungjun Lee [a], Jaebeom Lee [b,c,*], Chi-Ho Jeon [d], Young-Joo Lee [a,**]

[a] Department of Civil, Urban, Earth, and Environmental Engineering, Ulsan National Institute of Science and Technology (UNIST), Ulsan, 44919, Republic of Korea
[b] Division of Physical Metrology, Korea Research Institute of Standards and Science (KRISS), Daejeon, 34113, Republic of Korea
[c] Precision Measurement Major, University of Science and Technology (UST), Daejeon, 34113, Republic of Korea
[d] Department of Structural Engineering Research, Korea Institute of Civil Engineering and Building Technology (KICT), Goyang, 10223, Republic of Korea

ARTICLE INFO

Keywords:
Pitting corrosion
Corroded strands
Mechanical behavior
Probabilistic prediction
Surrogate model

ABSTRACT

This study proposes a probabilistic method for predicting the non-linear mechanical behavior of corroded steel strands. The proposed method follows a four-step process: (1) Developing sophisticated finite element models that accurately represent various types of corrosion; (2) Constructing a multi-surrogate model using Gaussian process regression; (3) Predicting load–displacement curves based on a theoretical model; and (4) Implementing a probabilistic analysis using Monte Carlo simulation and kernel density estimation. Validation was performed through two approaches: (i) scenario-based synthetic simulations of 1000 corrosion cases, and (ii) experimental tensile tests on 39 real-world corroded seven-wire strand specimens. Predictions closely matched experimental results, capturing tensile strength and yield displacement within 99 % prediction bounds for 94.87 % and 89.74 % of specimens, respectively. This framework provides an effective tool for assessing corroded strands, enabling the probabilistic evaluation of prestressed concrete girders and supporting maintenance strategies for corrosion-affected infrastructure.

1. Introduction

Steel strands are critical components of prestressed structures, such as prestressed concrete (PSC) bridges. The strands are exposed to various environmental factors throughout their service life. Corrosion is the primary factor affecting the physical appearance of these strands and their mechanical properties, as noted in references (Lee, 2022; Jeon et al., 2019; Biondini and Frangopol, 2018). This process results in cross-sectional loss within the strands. Therefore, it potentially degrades their tensile strength, reduces their stiffness, and compromises their ductility. Such degradation can severely affect the safety of PSC structures, leading to local yielding of the prestressing wires and brittle failure of the prestressed members (Jeon et al., 2020). Beyond the immediate structural damage, these failures can lead to catastrophic socioeconomic losses, increase safety concerns, and cause societal disruptions. For example, the Ynys-y-Gwas bridge in the UK, a single-span segmental bridge, collapsed suddenly in 1985 owing to the corrosion of its internal prestressed steel (Woodward and Williams, 1988). The Melle Bridge in Belgium fell in 1992 because of similar damage (De Schutter, 2013). Since the identification of corrosion in the Niles Channel Bridge in Florida, USA, in 1999, several other bridges across Virginia, Texas, Minnesota, Kansas, Indiana, and South Carolina have reported comparable issues. This has necessitated urgent inspections and repairs (Lee, 2022). Therefore, it is essential to reliably predict the mechanical behavior of corroded strands to evaluate the performance of these structures and formulate appropriate maintenance strategies.

One research direction to explain the mechanical behavior of corroded steel strands is to develop empirical models that estimate the yield and ultimate strengths using the experimental tensile test results of corroded wires. For example, Lu et al. (2016) developed a corrosion damage factor and bilinear constitutive model to define of corroded strands, capturing the effects of corrosion on the mechanical behavior. Zhang et al. (2017) proposed a similar bilinear model in which the mechanical properties decreased linearly with the cross-sectional corrosion loss up to a critical point, as defined by the experimental data. Notably, Zhang et al. (2019) introduced a stochastic bilinear stress–strain relationship that accounts for longitudinal variability using

This article is part of a special issue entitled: Novel Materials Testing published in Developments in the Built Environment.

* Corresponding author. Division of Physical Metrology, Korea Research Institute of Standards and Science (KRISS), Daejeon, 34113, Republic of Korea.
** Corresponding author. Department of Civil, Urban, Earth, and Environmental Engineering, Ulsan National Institute of Science and Technology (UNIST), Ulsan 44919, Republic of Korea.
E-mail addresses: jblee@kriss.re.kr (J. Lee), ylee@unist.ac.kr (Y.-J. Lee).

https://doi.org/10.1016/j.dibe.2025.100644
Received 13 December 2024; Received in revised form 13 February 2025; Accepted 11 March 2025
Available online 15 March 2025

cross-sectional data modeled through a probability distribution. Wang et al. (2020) demonstrated that although marginally corroded strands fit a bilinear model, those with critical corrosion losses transition into a single-linear model. Finally, Franceschini et al. (2022) introduced the CPS model, a trilinear constitutive model that predicts the mechanical behavior of corroded strands based on pit morphology, maximum pit depth, and cross-sectional and mass loss. However, one of the limitations of studies that rely on experimental data is the difficulty in creating test specimens that accurately represent various corrosion conditions. For example, it is particularly difficult to reproduce specific corrosion patterns, such as pitting with precise depth and distribution on the wire surface. Thus, the difficulties involved make it challenging to prepare specimens with the exact corrosion shapes and sizes desired for testing. These challenges can hinder the capability to obtain reliable and consistent data across corrosion scenarios.

Another research direction involves establishing estimation models based on data obtained from finite element (FE) models, rather than relying solely on experimental data. Ghoreishi et al. (2007) proposed a 3D FE model of a strand under static axial loads. They compared the results with those of various theoretical strand models to validate their approach. Judge et al. (2012) and Yu et al. (2014) developed detailed elastoplastic FE models designed specifically for steel strands. These provided insights into the material behavior under different loading conditions. Abdullah et al. (2016) developed an FE model detailing a prestressing strand's response to stress and dynamic post-breakage, assessing how the modeling parameters influence the behavior and load distribution. Jeon et al. (2019) proposed a bilinear strand model by integrating regression analysis to estimate the ultimate stress and strain properties, and adjusting the coefficients according to the pit configurations determined by FE analysis. Li et al. (2020) introduced an FE model that relates pit dimensions to reduced strength and increased stress concentration in steel wires. This emphasized the impact of microstructural defects on the overall performance. Chen et al. (2021) developed a 3D FE model of a multi-layered wire system to investigate the effect of pitting corrosion on the reduction in load-carrying capacity, providing crucial insights into the degradation mechanisms in corroded wires. This approach aims to address the limitations of experimental data-based studies by enabling researchers to generate a comprehensive set of data under various corrosion and loading conditions as intended. With FE models, it is feasible to simulate precise corrosion scenarios. These allow for the examination of a wider range of conditions that may be difficult or impractical to replicate experimentally.

However, irrespective of whether the research utilizes experimental data or data derived from FE models, inherent limitations exist in attempts to estimate the stress–strain or load–displacement relationship: (1) Similarly as generating experimental data can be expensive, designing detailed FE models and obtaining accurate analysis data also requires significant resources. It is crucial to acquire data across various corrosion conditions in advance. However, this presents the challenge of maximizing the utility of the data with a minimal number of samples. Therefore, well-designed experiments or simulations are necessary to ensure that the most informative and representative data are obtained. This enables accurate estimations while ensuring that the costs and resource use are manageable. (2) The focus is typically on providing estimation formulae for the yield or ultimate strength and strain of corroded steel strands. This generally simplifies the stress–strain curve to a bilinear or trilinear representation. Although this approach is sufficient for many applications, corrosion which generally increases the complexity of the mechanical behavior (Vu et al., 2009) necessitates models that can accurately capture these non-linear characteristics. Research that effectively simulates the full range of non-linear behaviors in corroded materials is relatively limited. Thus, the deficiency of comprehensive studies in this area can be a drawback when detailed and accurate modeling of the material response under various loading conditions is necessary. (3) Owing to the various uncertainties that can originate during the process of measuring corrosion and the heterogeneity of material properties, a probabilistic approach may be necessary to estimate the performance range of corroded steel strands. However, few studies have considered the uncertainties. The variability in corrosion measurement techniques and inherent non-uniformity of material properties can affect the accuracy of predictions, but many studies have focused on deterministic methods.

To address these challenges, Lee et al. (2020) proposed a probabilistic method for predicting the mechanical characteristics of corroded strands. This approach uses sophisticated FE analysis of corroded wires and theoretical strand models to estimate the ultimate tensile strength and strain of the corroded strands. Additionally, to reduce the computational cost of FE analysis for probabilistic analysis, a non-parametric surrogate model was developed using Gaussian process regression (GPR). The effectiveness of this method was demonstrated by its capability to predict probabilistic tensile test results for eight corroded steel strand specimens. Despite the achievements of Lee et al.'s method, it has certain limitations: (1) It focuses primarily on predicting the ultimate tensile strength and strain of corroded strands. This may limit its application in structural analyses, such as those for PSC girders or bridges, where a comprehensive understanding of the mechanical behavior is essential. (2) The method does not predict the yield strength or strain. This hinders the assessment of key performance indicators, such as the strength ratio (i.e., ultimate tensile strength/yield strength) and ductility ratio (i.e., ultimate strain/yield strain). These are critical when evaluating corrosion-induced cross-sectional loss. (3) The predictive model was validated using a relatively small sample (i.e., eight specimens). Further validation using a larger set of specimens is necessary to verify the reliability of the prediction model.

In this study, the method introduced by Lee et al. (2020) was developed further to enable probabilistic predictions of the mechanical behavior of corroded steel strands. This enhanced approach differs from existing methods in its use of the Ramberg–Osgood curve (Ramberg and Osgood, 1943) to capture the material behavior non-linearity without simplifying it or necessitating the definition of a critical cross-section for post-yield hardening consideration. Furthermore, it incorporates a sophisticated FE analysis of corroded wires, in conjunction with an advanced theoretical strand model that accounts for the mutual interactions between wires. To mitigate the high computational costs typically associated with probabilistic analyses, a multi-surrogate model approach employing GPR was integrated. This model effectively derived the load–displacement curve of the corroded wire relative to the degree of corrosion, in accordance with the Ramberg–Osgood curve. The robustness and predictive accuracy of the proposed method were validated using tensile test results from 39 corroded steel strand specimens provided by Jeon et al. (2023).

2. Proposed probabilistic prediction method for mechanical behavior of corroded strands

The proposed method for estimating the mechanical behavior of strands affected by corrosion is illustrated in Fig. 1. It includes the following four steps: (1) Development of sophisticated 3D FE models of corroded wires. These FE models are constructed to simulate the load–displacement behavior of corroded wires up to rupture, accounting for varying geometric properties such as types of corrosion, pit depth, and width. (2) Construction of a multi-surrogate model. A multi-surrogate model, informed by the FE analysis results, effectively captures the load–displacement response of corroded wires by employing machine learning algorithms including GPR. (3) Prediction of the load–displacement curve with uncertainties. A Monte Carlo simulation (MCS) is used to generate random samples. These are then utilized to estimate the load–displacement relationship of the corroded wires by incorporating the effects of corrosion and associated uncertainties. The estimated curve is subsequently input into the theoretical strand model to estimate the load–displacement curve for various combinations of samples. (4) Implementation of a probabilistic approach to assess the

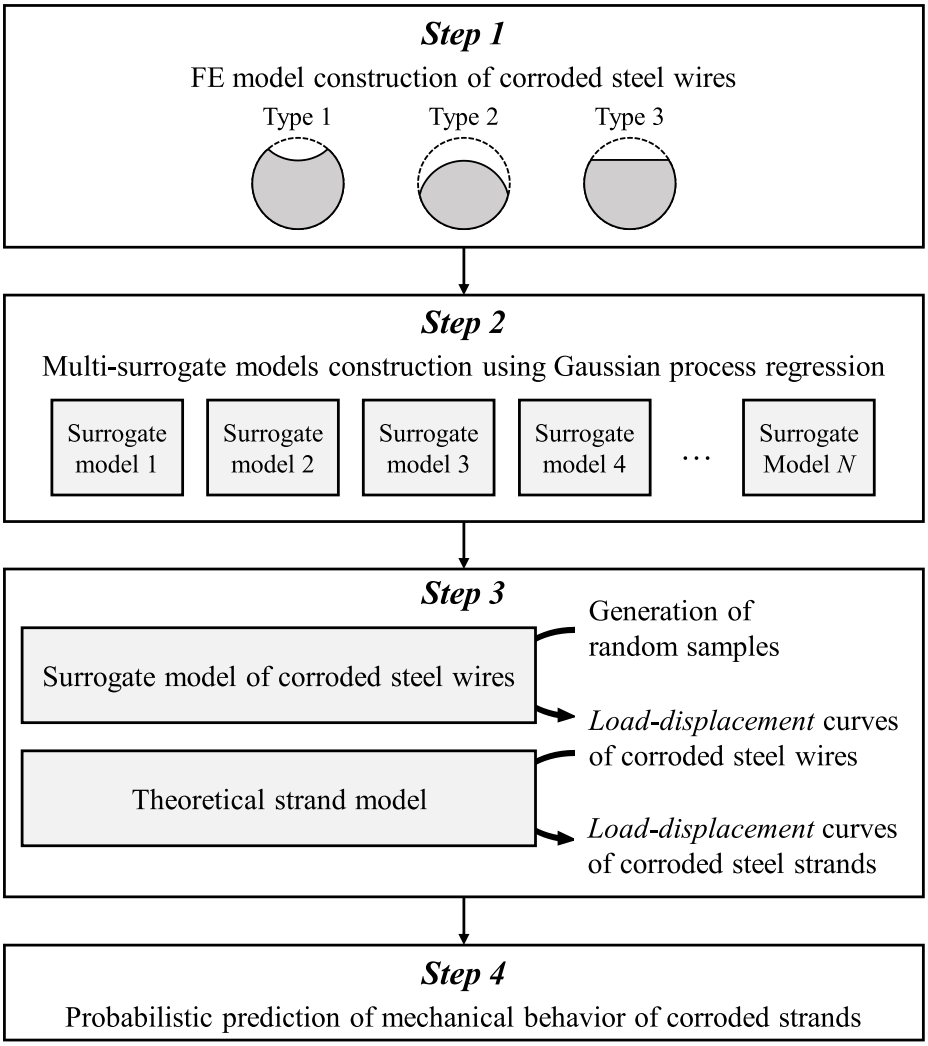

Fig. 1. Overview of the proposed probabilistic prediction method.

mechanical behavior of corroded strands. Using the kernel density estimation (KDE) method, the prediction bounds of the mechanical behavior of the corroded strands is determined, with results presented at a specified confidence level.

2.1. Step 1: development of 3D FE models of corroded wires

Before FE modeling, the degree of corrosion, a crucial parameter for evaluating the mechanical behavior of corroded wires, is assessed based on corrosion morphology, including pit depth and distribution patterns. For this task, high-precision techniques such as 3D laser scanning (Zhang et al., 2019; Franceschini et al., 2022) and scanning electron microscopy (SEM) (Wang et al., 2020; Liu et al., 2017, 2021) can provide highly detailed corrosion morphology, offering precise geometric characterizations of corroded wires. However, these methods can be time-consuming and costly, which may limit their practicality, particularly for inspections of in-service bridges. Moreover, developing FE models for all corrosion types based on such detailed morphological data is computationally demanding and difficult to generalize due to the complexity and variability of corrosion patterns. Thus, this study adopts an approach that simplifies corrosion morphology by utilizing pit depth as a key parameter for estimating section loss.

Jeon et al. (2019) proposed three types of corrosion shapes based on pit configurations to facilitate section loss calculations (Jeon et al., 2019). The pit configuration models (i.e., hemispherical, concave, and planar pits), derived from the observations of real corroded strands, are shown in Fig. 2. The corroded area is shown in white, while the remaining sectional area is shown in grey. The sectional loss of the wires (A_{SL}) can be obtained using Eqs. (1)–(6) for $0 \le d_p \le 2r$:

$$A_{SL,1} = 2r^2(\theta_1 - \sin\theta_1 \cos\theta_1) \tag{1}$$

$$\theta_1 = \arccos\left(1 - \frac{d_p}{2r}\right) \tag{2}$$

$$A_{SL,2} = r^2(2\theta_2 - \pi - 2\sin\theta_2 \cos\theta_2) \tag{3}$$

$$\theta_2 = \arccos\left(-\frac{d_p}{2r}\right) \tag{4}$$

$$A_{SL,3} = r^2(\theta_3 - \sin\theta_3 \cos\theta_3) \tag{5}$$

$$\theta_3 = \arccos\left(1 - \frac{d_p}{r}\right) \tag{6}$$

where $A_{SL,1-3}$ denote the sectional loss based on the type of the pit configuration model, d_p denotes the pit depth (i.e., the deepest depth), and r denotes the radius of the wire.

In this study, FE models of corroded steel wires were developed using the commercial software package ABAQUS. These models were constructed to reflect the pit depth and longitudinal width according to the

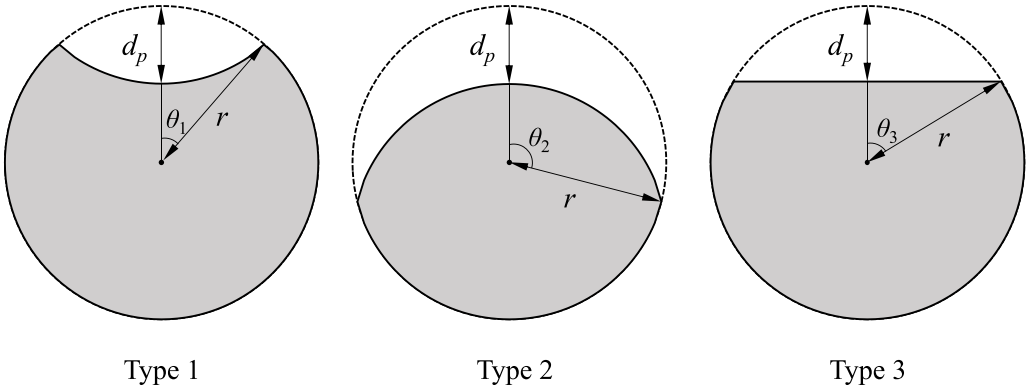

Fig. 2. Idealized pit configuration models of the corroded wire (Jeon et al., 2019).

pit configuration models shown in Fig. 3. FE models were developed for a range of pit depths, varying from 0.1 mm to 1.5 mm, and Fig. 3 represents each type of FE model with a pit depth of 1.0 mm. Further details on the FE model construction are available in previous studies (Jeon et al., 2019; Lee et al., 2020).

To enhance the accuracy of estimating the mechanical behavior of steel wires, it is essential to use an appropriate material model. Previous studies have typically employed bilinear or trilinear curves that simplify the representation of the non-linear behavior of steel wires. Such simplifications can pose challenges in capturing the non-linearity associated with the sectional loss owing to corrosion. This potentially causes inaccuracies in the estimation of the mechanical behavior of steel wires. Therefore, in this study, the stress–strain relationship for prestressing steel recommended by the *Probabilistic Model Code* (PMC) (JCSS, 2001) was adopted. Fig. 4 provides a typical stress (σ)–strain (ε) diagram for prestressing steel indicating the corresponding mechanical properties: tensile strength (f_u), proportional limit (f_{pl}), modulus of elasticity (E), and total elongation at maximum force (ε_u). In addition, prestressed steels exhibit a gradual yield transition (JCSS, 2001). Thus, the yield stress is determined based on the strain rate criterion. According to the European standard EN 10138-3 (EN 10138, 2009), the yield stress can be defined as the stress at a 0.1 % offset, also known as the 0.1 % proof stress ($f_{0.1}$). For cases that require an analytical expression for the stress–strain relationship, the PMC recommends the Ramberg–Osgood curve, which is characterized by three mechanical parameters:

$$\varepsilon = \frac{\sigma}{E} + p\left(\frac{\sigma}{f_{0.1}}\right)^q \tag{7}$$

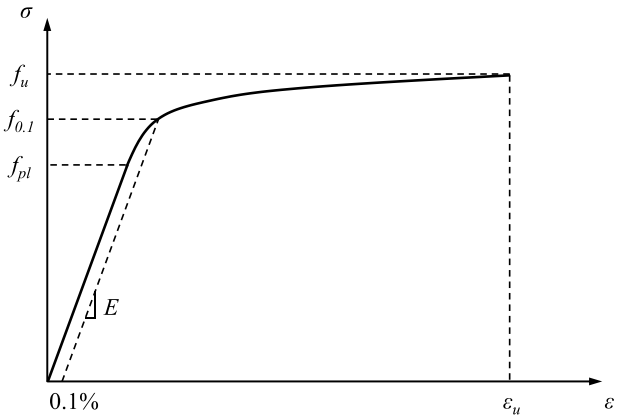

Fig. 4. Typical stress–strain diagram for a prestressing steel (JCSS, 2001).

where p is the plastic strain corresponding to $f_{0.1}$, which is defined as a constant value of 0.001. The strain hardening exponent (q) is a parameter that describes the rate at which a material hardens during plastic deformation. This parameter can be determined by fitting the Ramberg–Osgood curve to the ultimate point, which is characterized by the ultimate strain (ε_u) and tensile strength (f_u). In other words, q is calculated by considering both the elastic and plastic components of deformation, as shown in Eq. (8):

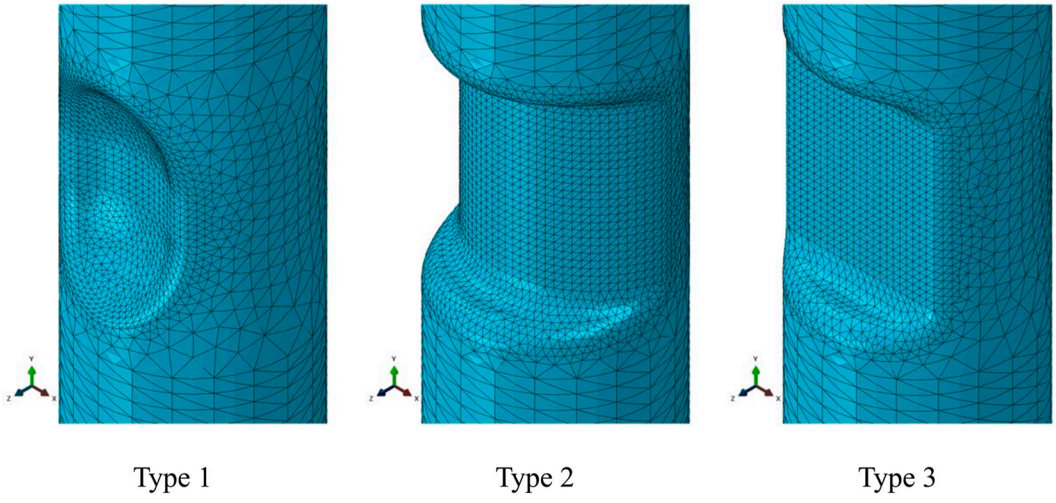

Fig. 3. Three types of FE models of corroded wires.

$$q = \frac{\ln((\varepsilon_u - (f_u/E))/p)}{\ln(f_u/f_{0.1})} \tag{8}$$

This equation captures the relationship between stress and strain beyond the elastic limit, providing insight into how a material resists further deformation after yielding. Therefore, using Eqs. (7) and (8), the defined Ramberg–Osgood material model can effectively capture the non-linearity of the mechanical behavior of steel wires. Additionally, random variables (RVs) can be introduced into the model. This enables the estimation of the material curve with uncertainties (JCSS, 2001; Jacinto et al., 2012). To implement the Ramberg–Osgood curve in ABAQUS, data conversion is essential. This process involves the transformation of engineering (i.e., nominal) stress–strain values into true stress–strain values, as detailed in Eqs. (9) and (10) (Systèmes, 2016). This transformation is important to ensure both compatibility and precision during simulations and subsequent analyses within the ABAQUS framework.

$$\sigma_{true} = \sigma_{eng}(1 + \varepsilon_{eng}) \tag{9}$$

$$\varepsilon_{true} = \ln(1 + \varepsilon_{eng}) \tag{10}$$

where σ_{true} and ε_{true} denote the true stress and strain. σ_{eng} and ε_{eng} denote the engineering stress and strain, respectively.

2.2. Step 2: multi-surrogate model construction using GPR

The mechanical behavior of the corroded wire can be determined using several sophisticated FE models constructed in *Step 1*. However, as mentioned earlier, the material properties, which are essential parameters for material models, are known to have uncertainties. To perform a probabilistic analysis that considers these uncertainties, repeated FE simulations, which incur high computational costs, are necessary for a sufficient number of samples for the given RVs. Therefore, this study introduces a surrogate model approach to cost-efficiently estimate the mechanical behavior of corroded wires, rather than relying on expensive FE simulations.

To construct a surrogate model, it is essential to first determine the design points at which the FE simulations are conducted. Employing design of experiment methodologies such as Latin hypercube sampling (LHS) can efficiently guide the selection of these points. This ensures comprehensive coverage of the design space and thereby, improves the accuracy of the surrogate model (McKay et al., 1979; Viana, 2016). LHS is a space-filling sampling method that generates P unique samples from a multi-dimensional distribution by dividing the samples into equally sized strata and sampling randomly within each stratum. The fundamental concept involves dividing the range of each of the d dimensions into P uniformly spaced intervals. Within each interval, a coordinate value is selected (randomly or at its center) to ensure a thorough representation of the entire distribution. This method generates P coordinate values for each dimension. To ensure the uniqueness of each sample, random permutation is applied to select the coordinate values from the intervals. Fig. 5 provides a clear visual illustration of the difference between two space-filling samplings with $d = 2$ dimensions and $P = 20$ samples. Fig. 5(a) displays random sampling with several clusters of samples. Fig. 5(b) demonstrates a more uniform distribution of samples across the design space afforded by LHS.

The next step is to conduct an FE simulation based on the LHS design points to generate data to construct a surrogate model that captures the relationship between the input variables and output responses. The Gaussian process (GP) has been widely adopted for this purpose. This is because it can model complex true functions based on a small number of function evaluations. The fundamental assumption of a surrogate model based on a GP is that the response to input $\boldsymbol{x}$ (represented as $y(\boldsymbol{x})$) is the realization of a GP (Rasmussen and Williams, 2005), which is defined as follows:

$$y(\boldsymbol{x}) \sim GP(m(\boldsymbol{x}), k(\boldsymbol{x}, \boldsymbol{x}'; \boldsymbol{\Omega})) \tag{11}$$

where $m(\boldsymbol{x})$ denotes the mean function (i.e., $\mathrm{E}[y(\boldsymbol{x})]$); $k(\boldsymbol{x}, \boldsymbol{x}')$ denotes the covariance function (i.e., $\mathrm{E}[(y(\boldsymbol{x}) - m(\boldsymbol{x}))(y(\boldsymbol{x}') - m(\boldsymbol{x}'))]$); and $\boldsymbol{\Omega}$ denotes a set of parameters that represent characteristics of GP, often referred to as hyperparameters. For example, the Matérn class covariance function (Rasmussen and Nickisch, 2015) adopted in this study is specified as

$$k(\boldsymbol{x}, \boldsymbol{x}'; \boldsymbol{\Omega}) = \omega_1 \frac{2^{1-\nu}}{\Gamma(\nu)} \left(\sqrt{2\nu} \ \frac{\|\boldsymbol{x} - \boldsymbol{x}'\|}{\omega_2} \right)^{\nu} K_\nu \left(\sqrt{2\nu} \ \frac{\|\boldsymbol{x} - \boldsymbol{x}'\|}{\omega_2} \right) \tag{12}$$

where $||\boldsymbol{x} - \boldsymbol{x}'||$ represents the distance between the two inputs $\boldsymbol{x}$ and $\boldsymbol{x}'$; ω_1 and ω_2 are hyperparameters in $\boldsymbol{\Omega}$; Γ is Euler's Gamma function; K_ν is the modified Bessel function of the second type; and ν is the shape parameter with a constant value of 5/2 (i.e., the *Matérn 5/2 kernel*).

A dataset matrix ($\mathbf{D}$) consisting of an input matrix ($\mathbf{X}$) and output vector ($\mathbf{y}$) can be represented by the following expression:

$$\mathbf{D} = \{(\mathbf{X}, \mathbf{y})\} = \left\{ (x_{ij}, y_i) \middle| i = 1, \ldots, N_D; \ \ j = 1, \ldots, N_{RV} \right\} \tag{13}$$

where N_D denotes the number of design points defined by the LHS, N_{RV} denotes the number of RVs, x_{ij} denotes the j-th RV at the i-th design point, and y_i denotes the outcome of the FE analysis at the i-th design point. The maximum likelihood estimation method is often employed to determine the optimal hyperparameters of the covariance function (denoted as $\widehat{\boldsymbol{\Omega}}$) of the GP (Rasmussen and Nickisch, 2015). This method focuses on maximizing the likelihood of the observed dataset, which is expressed as a conditional probability density function (PDF) associated with the multivariate Gaussian distribution, as demonstrated below:

$$\widehat{\boldsymbol{\Omega}} = \underset{\boldsymbol{\Omega}}{\operatorname{argmax}} \ln p(\mathbf{y}|\mathbf{x}, \boldsymbol{\Omega}) \tag{14}$$

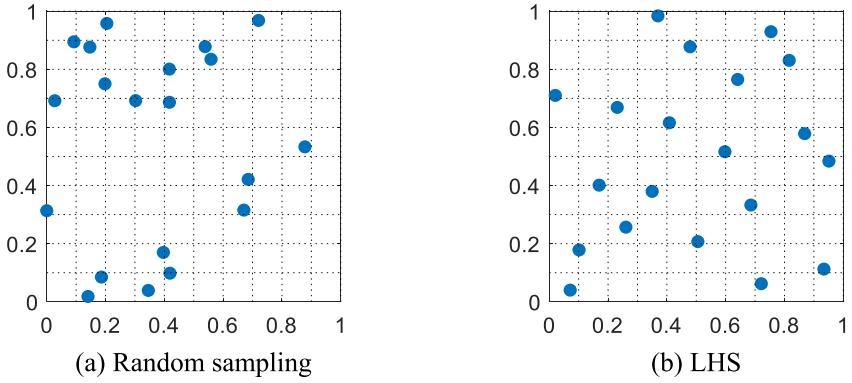

Fig. 5. Examples of space-filling samplings with two dimensions and 20 samples.

$$\ln p(\mathbf{y}|\mathbf{x},\boldsymbol{\Omega}) = -\frac{1}{2}\mathbf{y}^{\mathrm{T}}\mathbf{K}^{-1}\mathbf{y} - \frac{1}{2}\log|\mathbf{K}| - \frac{N_D}{2}\ln(2\pi) \tag{15}$$

where $\mathbf{K}$ denotes the covariance matrix corresponding to the design point x_{ij}. After the model parameters have been estimated, the GP-based regression model (i.e., GPR) can be used to predict the response of an unknown input variable. For a new point ($\mathbf{X}_*$), GPR provides an estimated response ($\mathbf{y}_*$), characterized by the conditional mean $\mu_{\mathbf{y}}$ ($\mathbf{X}_*$) and variance $\sigma^2_{\mathbf{y}}(\mathbf{X}_*)$ of the Gaussian distribution:

$$p(\mathbf{y}_*|\mathbf{X}_*,\mathbf{X},\mathbf{y},\widehat{\boldsymbol{\Omega}}) \sim N\left(\mu_{\mathbf{y}}(\mathbf{X}_*),\sigma^2_{\mathbf{y}}(\mathbf{X}_*)\right) \tag{16}$$

$$\mu_{\mathbf{y}}(\mathbf{X}_*) = m(\mathbf{X}_*) + \mathbf{K}_*^{\mathrm{T}}\mathbf{K}^{-1}(\mathbf{y} - m(\mathbf{X})) \tag{17}$$

$$\sigma^2_{\mathbf{y}}(\mathbf{X}_*) = \mathbf{K}_{**} - \mathbf{K}_*^{\mathrm{T}}\mathbf{K}^{-1}\mathbf{K}_* \tag{18}$$

where $\mathbf{K}_*$ denotes the covariance matrix between the prediction ($\mathbf{X}_*$) and given input ($\mathbf{X}$). $\mathbf{K}_{**}$ denotes the covariance matrix for the predictive input matrix ($\mathbf{X}_*$).

In the process of estimating the mechanical behavior of a corroded wire using a surrogate model, predicting the entire behavior with a single surrogate model can be limited. To address this, we constructed multiple surrogate models to effectively represent the intricate non-linear behavior. This is described in *Step 2* of Fig. 1. This multi-surrogate model approach represents the entire system by decomposing it into several subsystems. Each of these subsystems is then represented by its specific surrogate model, which is characterized by more manageable inputs and outputs. For example, the continuous mechanical behavior curve of a corroded wire obtained from the FE simulation is divided into N points. Then, N surrogate models are constructed using GPR to represent each of the structural responses, specifically load and displacement. To further illustrate this approach, Fig. 6 compares the single surrogate model with the multi-surrogate model. As shown in Fig. 6(a), the single surrogate model estimates the mechanical properties at certain points but is unable to capture the entire behavior curve comprehensively. In contrast, Fig. 6(b) represents the multi-surrogate approach. This approach constructs N surrogate models for individual points along the curve, which together represent the entire non-linear behavior. This division allows for a more accurate representation of the complex, non-linear structural responses. In this study, the value of N is set to 100 to accurately capture the non-linearity of the curve. For simplicity, the mechanical behavior of the corroded wire can be approximated as bilinear for $N = 2$ and trilinear for $N = 3$. In addition, the *lsqcurvefit* function in MATLAB is used to estimate the non-linear curve. Employing the Ramberg–Osgood model, Eq. (7), we verified the absence of discontinuity in the mechanical behavior estimated using the multi-surrogate model.

2.3. Step 3: prediction of load–displacement curves for corroded steel strands

In *Step 3*, as shown in Fig. 1, MCS is used to generate random samples to address the inherent uncertainties in the material properties. After generating these samples, the load–displacement curve for the corroded wire is estimated for each sample using the multi-surrogate model developed in *Step 2*. This process yielded various load–displacement curves, each corresponding to a specific random sample. Subsequently, the estimated structural behavior of the corroded wire is employed to calculate the load–displacement curve using the theoretical strand model. This approach is essential to effectively reflect the structural complexity of the strand. By integrating these procedures, the behavior of the strand under various corrosion conditions can be assessed more accurately while accounting for the uncertainty. This section provides a detailed understanding of the theoretical strand model introduced in this study. It includes its foundational principles and analytical expressions.

Steel strands are composed of a straight core wire with radius r_c surrounded by several helical wires with radius r_h, each twisted at a specific *lay angle* α. This is shown in Fig. 7. A typical configuration is a seven-wire strand. Herein, the core wire is encircled by six helical wires. This intricate arrangement is characterized by complex interactions and geometries. It poses challenges in assessing the mechanical behavior of steel strands. Numerous theoretical models have been proposed to address this complexity (Spak et al., 2013), notably Costello's strand model (Costello, 1997). It is based on the thin-rod theory, which is widely approved.

The mechanical behavior of the strand is represented by integrating multiple wires in Costello's strand model, where each wire is considered as a thin rod that contributes to the overall behavior of the strand. This integration is based on the FE simulation results of the corroded wires, as detailed in *Steps 1* and *2*. The model emphasizes the strand geometry as a critical factor. It calculates the bending stiffness by summing the stiffness of individual wires and assuming the absence of friction or interaction between the wires. By incorporating the force and moment equations derived from the wire segments and combining these with a stiffness matrix that includes strand properties, such as curvature and torsion, the model provides comprehensive insights into the structural response of strands. However, in this study, we introduced the contact model proposed by Gnanavel and Parthasarathy (2012). It considers the interwire effects and friction based on Costello's model. Specifically, this model employs a *combined contact approach*, wherein each wire is in contact with all the other wires, as shown in Fig. 7.

Fig. 8 illustrates the global coordinate system {$\boldsymbol{x}$, $\boldsymbol{y}$, $\boldsymbol{z}$} and local coordinate system {$\boldsymbol{t}$, $\boldsymbol{n}$, $\boldsymbol{b}$}. These represent the right-hand Frenet–Serret system. The systems correspond to tangential, normal, and binormal unit vectors. The geometric relationship between the global and local coordinate systems is expressed as follows:

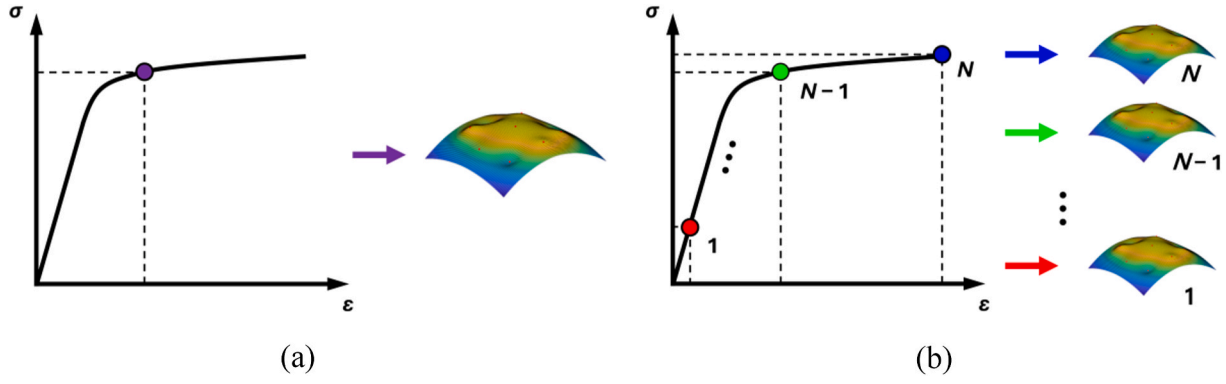

Fig. 6. Schematic representation of a generic mechanical behavior of corroded wire with: (a) single surrogate model and (b) multi-surrogate model.

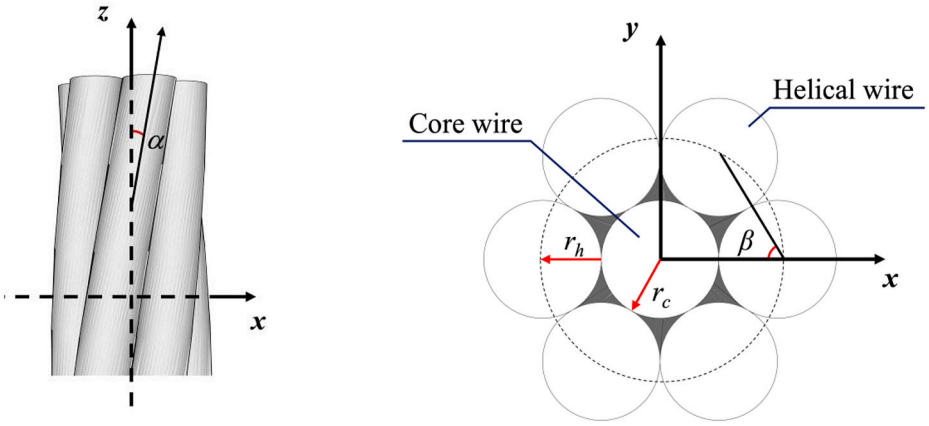

Fig. 7. A seven-wire steel strand with cross-section.

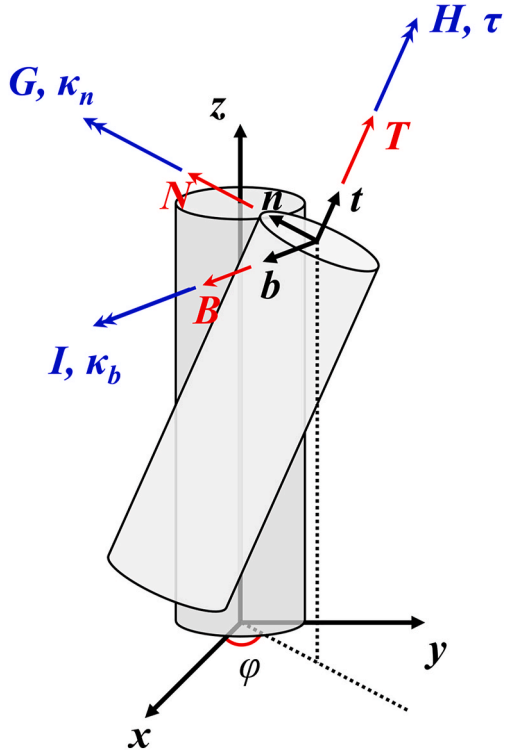

Fig. 8. Global and local coordinate systems and force components for core and helical wires.

$$\begin{pmatrix} \boldsymbol{n} \\ \boldsymbol{b} \\ \boldsymbol{t} \end{pmatrix} = \begin{pmatrix} -\cos\varphi & -\sin\varphi & 0 \\ \sin\varphi\cos\alpha & -\cos\varphi\cos\alpha & \sin\alpha \\ -\sin\varphi\cos\alpha & \cos\varphi\cos\alpha & \cos\alpha \end{pmatrix} \begin{pmatrix} \boldsymbol{x} \\ \boldsymbol{y} \\ \boldsymbol{z} \end{pmatrix} \tag{19}$$

where φ is the azimuth angle, indicating a counterclockwise rotation from the positive $\boldsymbol{x}$-axis and representing a helix around the central axis of a helical wire. During the decomposition of the wire force within an orthogonal framework, the force is split into components along the tangential ($\boldsymbol{T}$), normal ($\boldsymbol{N}$), and binormal ($\boldsymbol{B}$) axes. To understand the mechanical behavior of a strand, it is crucial to compute its tensile force ($\boldsymbol{F_z}$) along the global $\boldsymbol{z}$-axis.

For the core wire, where the local and global coordinates align, the tensile force is the tangential force ($\boldsymbol{T}$). This is because the normal ($\boldsymbol{N}$) and bi-normal ($\boldsymbol{B}$) forces are orthogonal to the $\boldsymbol{z}$-axis and have no effect. However, for helical wires, the binormal force ($\boldsymbol{B}$) is not stringently orthogonal to the $\boldsymbol{z}$-axis. Thus, it can affect the tensile force of the strand.

Therefore, the strand tension ($\boldsymbol{F}_{\boldsymbol{z},strand}$) can be expressed as

$$\boldsymbol{F}_{\boldsymbol{z},strand} = \boldsymbol{F}_{\boldsymbol{z},core} + \sum_{i=1}^{m} \boldsymbol{F}^i_{\boldsymbol{z},hel} \tag{20}$$

where $\boldsymbol{F}_{\boldsymbol{z},core}$ represents the axial force within the core wire, m denotes the number of helical wires, and $\boldsymbol{F}^i_{\boldsymbol{z},hel}$ are the axial forces in the i-th helical wire. The axial force in the core wire $\boldsymbol{F}_{\boldsymbol{z},core}$ consists of the tangential force ($\boldsymbol{T}_c$), and is computed as follows:

$$\boldsymbol{F}_{\boldsymbol{z},core} = \boldsymbol{T}_c = \int_{A_c} \sigma_c(\varepsilon_c) dA \tag{21}$$

where A_c is the cross-sectional area of the core wire, σ_c denotes the stress estimated using the constructed surrogate model, and ε_c represents the axial strain of the core wire. The axial force of the core wire is affected by the lateral contact conditions and Poisson's effect. Thus, ε_c can be calculated as

$$\varepsilon_c = \left(\frac{1 - \nu_c + 2\nu_c^2}{1 + \nu_c}\right)\varepsilon_s \tag{22}$$

where ν_c is the Poisson's ratio of the core wire and ε_s is the axial strain of the strand. However, to determine the axial force in the i-th helical wire $\boldsymbol{F}^i_{\boldsymbol{z},hel}$, it is necessary to consider both tangential component, $\boldsymbol{T}$, and binormal component, $\boldsymbol{B}$, in conjunction with the *lay angle* (α):

$$\boldsymbol{F}^i_{\boldsymbol{z},hel} = \boldsymbol{T}^i_h \sin(\alpha) + \boldsymbol{B}^i_h \cos(\alpha) \tag{23}$$

where $\boldsymbol{T}^i_h$ and $\boldsymbol{B}^i_h$ denote the tangential and binormal components of the force of the i-th helical wire, respectively. The calculation of the tangential force for the helical wires adopts the form:

$$\boldsymbol{T}^i_h = \int_{A^i_h} \sigma^i_h(\varepsilon_s) dA \tag{24}$$

where A^i_h is the cross-sectional area of the i-th helical wire and σ^i_h is the stress for the i-th helical wire as estimated by the surrogate model. The binormal force for the helical wires is also influenced by the interaction with adjacent wires, is given by

$$\boldsymbol{B}^i_h = \frac{-\boldsymbol{I}(r_h\boldsymbol{\tau}^2 + r_h\boldsymbol{\tau}\boldsymbol{\kappa_b} + \boldsymbol{\tau}) + \boldsymbol{H}(r_h\boldsymbol{\kappa_b} + r_h\boldsymbol{\tau}\boldsymbol{\kappa_b} + \boldsymbol{\kappa_b}) - \boldsymbol{T}r_h\boldsymbol{\kappa_b}\sin(\beta)}{\mu r_h\boldsymbol{\tau}\sin(\beta) + r_h\boldsymbol{\tau} + r_h\boldsymbol{\kappa_b} + 1} \tag{25}$$

where $\boldsymbol{I}$ and $\boldsymbol{H}$ are the binormal and tangential moments, respectively; $\boldsymbol{\tau}$ denotes the twist; $\boldsymbol{\kappa_b}$ denotes the binormal curvature; μ denotes the coefficient of friction; and β denotes the wire contact angle as depicted in Fig. 7 μ is defined as a constant value of 0.115 (Judge et al., 2012).

Further details regarding the interfacial contact forces of the strand are presented in Gnanavel and Parthasarathy (2012).

2.4. Step 4: probabilistic prediction of mechanical behavior of corroded steel strands

As described in *Steps 1–3*, the load–displacement of the steel strand is determined by the number of random samples generated using the MCS. These estimated curves vary within certain ranges of load and displacement. To define a probabilistic boundary for these results at a specified confidence level, the KDE method is utilized. This was proposed by Rosenblatt (1956) and Parzen (1962). The KDE non-parametrically estimates the PDF in a multi-variate form for load and displacement. This approach provides a smoother representation of the data distribution.

Given a dataset $\mathbf{u} = [u_1, u_2, \ldots, u_s]$, the PDF estimated using the KDE is represented as follows:

$$g(u) = \frac{1}{sh}\sum_{i=1}^{s} K\left(\frac{u-u_i}{h}\right) \tag{26}$$

where $g(u)$ is the estimated density at point u; K is the kernel function that assigns weights around data points; s is the number of data points; u is the point where the PDF is estimated; and u_i is the i-th data point; and h is the bandwidth coefficient, which is optimally determined following Silverman (2018). In this study, we estimated the PDF using a Gaussian kernel (Silverman, 2018) with zero mean and unit variance, as follows:

$$\widehat{g}(u) = \frac{1}{sh\sqrt{2\pi}}\sum_{i=1}^{s} e^{-\frac{(u-u_i)^2}{2h^2}} \tag{27}$$

For example, Fig. 9 shows the load–displacement curves predicted by the proposed method for a non-corroded strand. It emphasizes the distinct aspects of the behavior at various stages up to the ultimate displacement (D_u) for each sampling curve. The vertical and horizontal axes represent the load (i.e., axial force) in kN and displacement in mm, respectively. The grey curves represent individual predicted load–displacement outcomes, reflecting variability due to inherent uncertainties in input variables (e.g., material properties, geometric variations). The solid black line indicates the median of the predictions (i.e., the median of the grey curves). The scattered blue dots represent specific prediction points, provide a detailed view of the predictions, and reveal areas with high data density. The elliptical outlines show the prediction bounds estimated by KDE. Here, the inner ellipse typically represents the 50 % prediction interval, and the outer ellipse corresponds to the 95 % prediction interval. Fig. 9(a)–(c) systematically illustrate the load–displacement behavior at progressive stages: initial linear-to-nonlinear transition, hardening behavior, and full progression to ultimate displacement.

3. Illustrative example: scenario-based corrosion of strands

This section focuses on verifying the proposed method by applying it to probabilistically estimate the mechanical behavior of corroded strands under various corrosion scenarios. Initially, the key parameters and assumptions utilized in the corrosion scenarios are outlined briefly, including the number of corroded wires, pit corrosion types, extent of corrosion (i.e., pit depth), and uncertainty factors in the material properties considered. Subsequently, the proposed method is applied step-by-step to 1000 corrosion scenarios to illustrate how varying degrees of corrosion affect the mechanical behavior of strands, including tensile strength and displacement. Finally, the predicted results are analyzed to assess the validity and effectiveness of the proposed method under various corrosion conditions.

3.1. Corrosion scenarios of strands

In this study, corrosion scenarios focused on the cases of seven-wire strands commonly used in various structural applications. The strand consisted of a central core wire and six helically wound outer wires (Fig. 7). The core wire had a radius of 2.58 mm, while each helical wire had a radius of 2.50 mm. This resulted in an uncorroded cross-sectional area of 138.72 mm^2. For simplicity, corrosion was assumed to occur exclusively in helical wires as they are typically exposed to more aggressive environments (Darmawan and Stewart, 2007). Additionally, it was assumed that the mechanical behavior of corroded strands is primarily influenced by the cross-section with the most severe material loss due to corrosion, where stress concentration is expected to be most significant (Liu et al., 2017, 2021). Thus, the longitudinal variation in corrosion along the strand was not considered in this study.

Several key parameters were defined to systematically investigate the impact of corrosion on the mechanical behavior of the strands. The scenarios varied in terms of the number of helical wires affected by corrosion, ranging from none to all six. This variation enabled the assessment of the influence of different degrees of corrosion on the overall performance of the strands. Additionally, three types of pitting corrosion (hemispherical, concave, and planar pits) were considered to simulate realistic degradation patterns, wherein each affected the mechanical performance of the wires differently. The corrosion extent is quantified by parameters including the pit depth and cross-sectional area reduction. The pit depths range from 0.1 mm to 1.5 mm to address various severity levels. Moreover, the inherent uncertainty factors in material properties due to variations in quality and manufacturing processes are accounted for using probabilistic distributions. This approach provides a comprehensive analysis of how these variations affect the strand behavior. Each corrosion scenario was simulated using the proposed probabilistic method, which accounts for the random characteristic of the corrosion and material properties. By

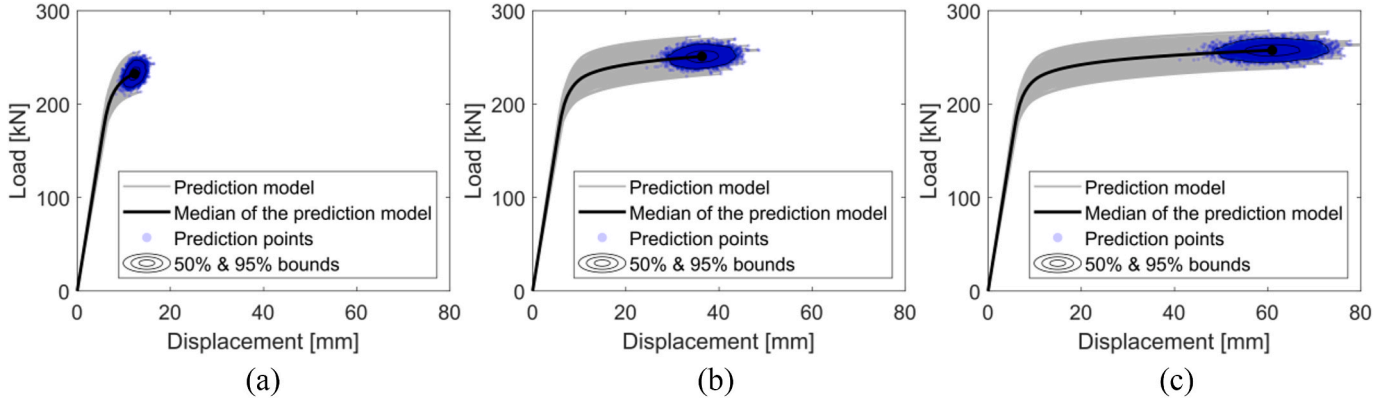

Fig. 9. Probabilistic prediction example for the load–displacement curves of a strand at (a) $0.2D_u$; (b) $0.6D_u$; and (c) D_u.

applying this method to 1000 distinct scenarios, we observed the distribution of mechanical behavior outcomes such as tensile strength and displacement, and evaluated how these outcomes fell within the prediction bounds for different degrees and types of corrosion.

For example, the determination of the corrosion scenarios follows a structured and systematic process designed to verify the proposed method by accurately capturing the variability and randomness inherent in the corrosion process.

(1) Setting the number of corroded wires (N_{cw}): The number of helical wires affected by corrosion was selected by drawing an integer from a uniform distribution between 0 and 6. For example, if $N_{cw} = 3$, three of the six helical wires were considered to be corroded, and the remaining were assumed to be non-corroded.
(2) Assigning the pit types (PT): Each corroded wire was assigned a corrosion type selected from three predefined categories: Type 1 (hemispherical pits), Type 2 (concave pits), and Type 3 (planar pits). With N_{cw} set to 3, an example outcome could be PT = [3, 2, 2, 0, 0, 0]. It indicates that the first wire had Type 3 corrosion, the second and third wires had Type 2 corrosion, and the remaining wires were non-corroded.
(3) Determining pit depth: For each corroded wire (i.e., where PT is not 0), the pit depth was selected from a uniform distribution between 0.0 mm and 1.5 mm. For example, in the case of PT = [3, 2, 2, 0, 0, 0], the pit depth (d_p) could be d_p = [1.18, 0.42, 0.63, 0, 0, 0]. Here, only the corroded wires have assigned pit depths. A_{SL} was calculated using Eqs. (1)–(6). These model the relationship between the pit depth and cross-sectional area reduction.

After the corrosion scenario was defined fully by the number of corroded wires, their corrosion types, and corresponding pit depths, the analyses were performed using the proposed method. A total of 1000 corrosion scenarios were systematically defined and analyzed through Processes (1)–(3) to comprehensively evaluate the mechanical behavior of the strands under varying conditions.

3.2. Analysis results

The proposed method considers corrosion scenarios and material uncertainties as inputs. To address these uncertainties, MCS was employed to generate 10,000 random samples for probabilistic predictions. The RVs considered in this study include the ultimate tensile strength (f_u), ultimate strain (ε_u), elastic modulus (E), and yield strength (f_y) of the steel wire. Their statistical properties are detailed in Table 1. These RVs have been investigated extensively based on the literature (Lee et al., 2020; JCSS, 2001; Jacinto et al., 2012). Using these samples, the multi-surrogate model was then constructed as described in Section 2.2 to estimate the load–displacement curves of the corroded wires for each corrosion scenario. This process yielded 70,000 load–displacement curves corresponding to a single-core wire and six helical wires for each scenario. Finally, the estimated structural behavior of the corroded wires was used to calculate the load–displacement curves of the strands using a theoretical strand model (Gnanavel and Parthasarathy, 2012). The strand geometry, including a length of L of 800 mm and α of 8° for helical wires (Fig. 7), was also considered in the modeling.

Table 1
Statistical properties of RVs in material properties.

RV	Mean	Coefficient of variation	Distribution type	Correlation coefficient			
				f_u	ε_u	E	f_y
f_u	1865 MPa	0.020	Normal	1.0			Sym.
ε_u	0.075	0.080	Normal	0.07	1.0		
E	195 GPa	0.025	Normal	0	0	1.0	
f_y	$0.85f_u$ MPa	0.030	Normal	0.78	0	0	1.0

The prediction bounds in Section 2.4 were conducted based on 10,000 strand samples for each of the 1000 corrosion scenarios. To illustrate a range of feasible outcomes, four representative scenarios (i.e., corresponding to non-corroded, minor corrosion, moderate corrosion, and severe corrosion cases) were selected. Table 2 excerpted these scenarios. It categorizes these by their specific characteristics including N_{cw}, PT, d_p, and the ratio of the corroded to nominal wire cross-sectional area (η_w). Specifically, in Scenario 166, which represents the non-corroded case, no corrosion was observed in any of the wires. In Scenario 312, minor corrosion was evident. Here, wire W_1 showed a pitting depth of 0.51 mm and reduction in cross-sectional area of 3.85 %. Moderate corrosion was observed in Scenario 529. Here, three wires (W_1, W_2, and W_3) were affected. W_1 experienced the most severe corrosion. This is reflected by a pitting depth of 0.91 mm and decrease in cross-sectional area of 9.06 %. Finally, Scenario 795 demonstrated severe corrosion. All the six wires were damaged to varying degrees. The most affected was wire W_4, which had a pitting depth of 1.10 mm and reduction in cross-sectional area of 27.78 %.

Fig. 10 presents the probabilistic prediction results of the load–displacement curves for the four selected corrosion scenarios. In this model, the ultimate strength is defined as the load at which the first of the seven wires ruptures. The ultimate displacement refers to the displacement at that point. The red dotted line represents the independently sampled test scenario used for comparison with the predictive model. As the corrosion level increased across the four scenarios, a decreasing trend in structural performance became evident. The non-corroded strands showed a gradual transition from linear to non-linear behavior, whereas both ultimate strength and displacement decreased progressively as the corrosion deteriorated. With minor corrosion, this transition occurred earlier, and the load-bearing capacity reduced. Additionally, the reduction in cross-sectional area due to corrosion led to a decrease in stiffness, reflected in a lower slope in the elastic region of the load–displacement curve. As corrosion became more severe, strand performance further deteriorated, displaying earlier transitions to non-linearity, reduced stiffness, and lower strength. These results clearly demonstrate the detrimental effects of increased corrosion on the load-bearing capacity and ductility of the strands.

Table 2
Selected corrosion scenarios of strand.

Scenario ID	N_{cw}	Wire	PT	d_p (mm)	η_w (%)
166	0	W_1	–	0.00	0.00
		W_2	–	0.00	0.00
		W_3	–	0.00	0.00
		W_4	–	0.00	0.00
		W_5	–	0.00	0.00
		W_6	–	0.00	0.00
312	1	W_1	1	0.51	3.85
		W_2	–	0.00	0.00
		W_3	–	0.00	0.00
		W_4	–	0.00	0.00
		W_5	–	0.00	0.00
		W_6	–	0.00	0.00
529	3	W_1	3	0.80	10.33
		W_2	2	0.19	4.84
		W_3	1	0.91	9.06
		W_4	–	0.00	0.00
		W_5	–	0.00	0.00
		W_6	–	0.00	0.00
795	6	W_1	1	1.40	17.02
		W_2	3	0.12	0.63
		W_3	1	0.23	1.18
		W_4	2	1.10	27.78
		W_5	1	0.17	0.75
		W_6	3	0.73	9.04

$\eta_w = A_{SL}/A_{w0}$; A_{w0} is the cross-sectional area of the nominal wire.

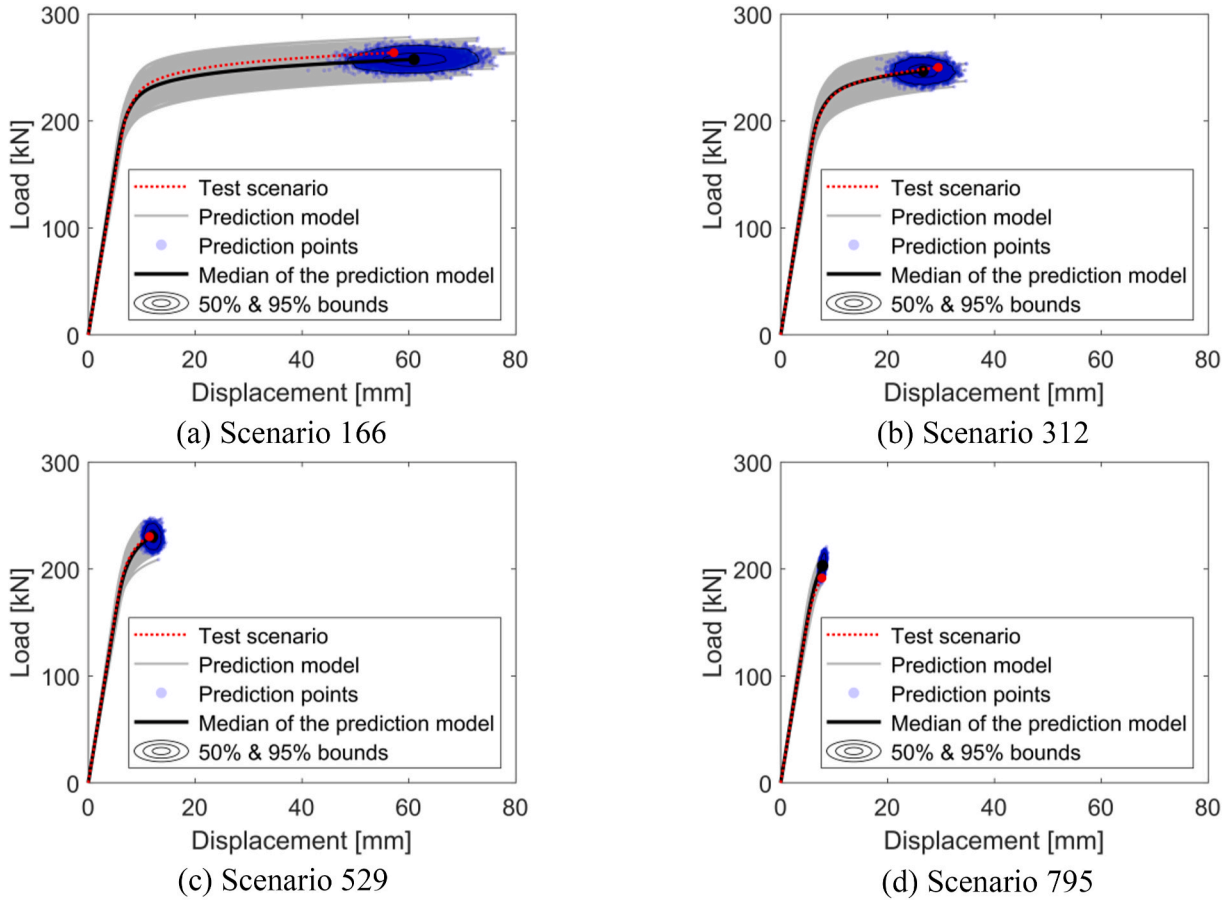

Fig. 10. Probabilistic prediction results of load–displacement curves for selected corrosion scenarios.

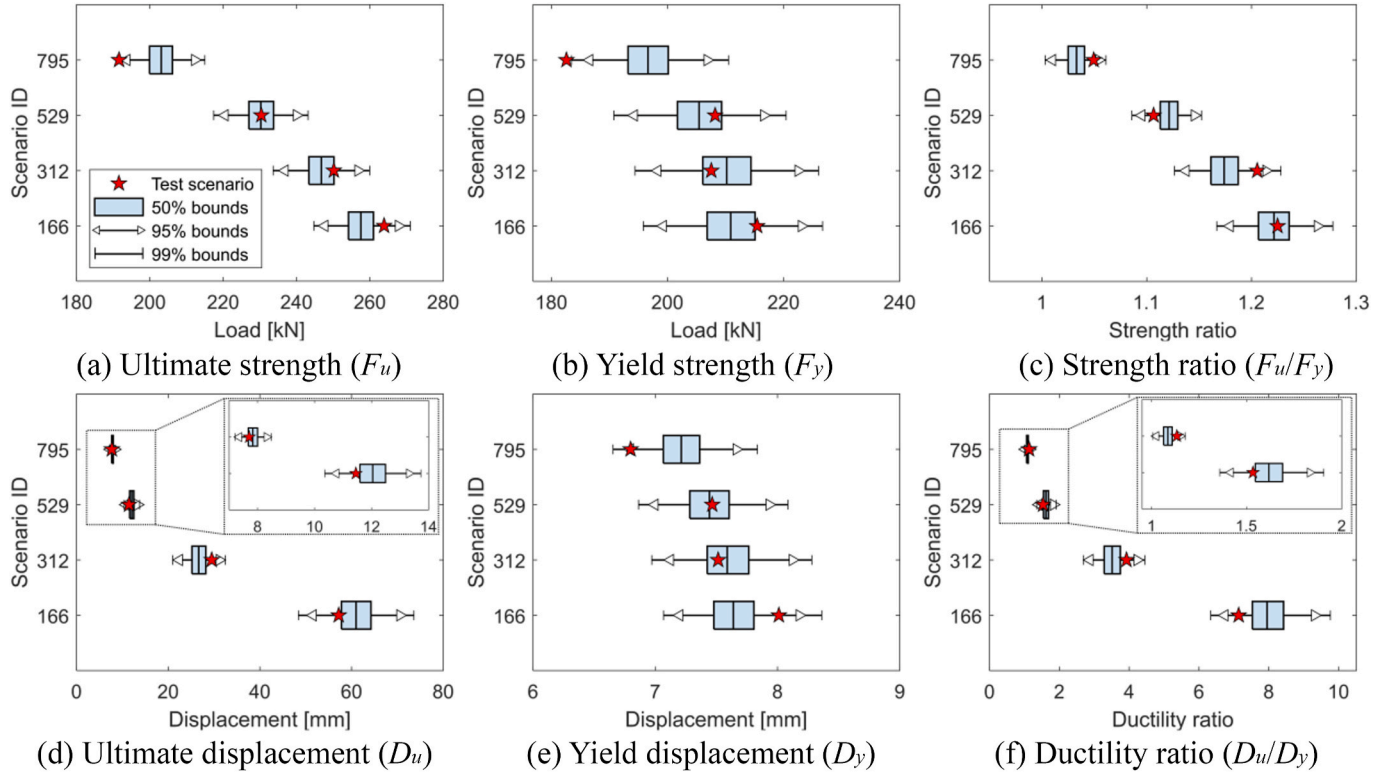

Fig. 11. Probabilistic prediction bounds compared with test scenario for the mechanical properties of selected corrosion scenarios.

Furthermore, the analysis outcomes show the effectiveness of the proposed method in probabilistically predicting the load–displacement behavior under the given corrosion scenarios. Fig. 11 shows box plots of the key mechanical properties (i.e., ultimate strength (F_u), yield strength (F_y), strength ratio (F_u/F_y), ultimate displacement (D_u), yield displacement (D_y), and ductility ratio (D_u/D_y)) across the four corrosion scenarios. Previously mentioned, the ultimate points represent the first rupture of the wires. Meanwhile, the yielding points were calculated using a 0.1 % offset method applied to the load–displacement curve, according to the PMC guidelines (JCSS, 2001). Each box plot displays the 50 %, 95 %, and 99 % prediction bounds for the corrosion scenarios. The red stars represent the test scenarios. These plots clearly illustrate how the test scenarios fall within the prediction bounds, facilitating an effective comparison. Based on this, 1000 corrosion scenarios were analyzed to verify the proposed method. Table 3 summarizes the results and shows the number of scenarios that fell within each prediction bounds. The majority of the 1000 scenarios were within the 50 %, 95 %, and 99 % bounds of the mechanical properties. For the ultimate strength, 954 of the 1000 scenarios fell within the 95 % bounds, and 988 (98.8 %) fell within the 99 % bounds. Similarly, for the ductility ratio, 962 of the 1000 scenarios fell within the 95 % bounds, and 994 (99.4 %) were within the 99 % bounds. Although a few properties showed marginally more variability within the 50 % bounds, the method effectively captured the majority of the mechanical properties across wider ranges. These results verify the robustness of the proposed method in accurately capturing the probabilistic distribution of mechanical properties under different corrosion scenarios.

4. Application example: field-corroded strand specimens

4.1. Test specimens

The proposed method was tested on strand specimens collected from the external tendons of in-service PSC box bridges that had been exposed to natural environmental conditions over time, leading to varying degrees of corrosion (Jeon et al., 2023). As shown in Fig. 12(a), the collected test specimens included both non-corroded and corroded strands. Jeon et al. (2019) proposed a deterministic method for estimating the load and displacement of corroded strands using a bilinear constitutive model. Meanwhile, Lee et al. (2020) introduced a probabilistic approach to predict the ultimate load and displacement. The proposed method was evaluated by comparing its probabilistic predictions with actual measurements from 39 stranded specimens, including specimens from previous studies. The test specimens are seven-wire strands consisting of one core wire surrounded by six helical wires. Among the 39 specimens, two are non-corroded strands and 37 are corroded ones. All these have a nominal diameter of 15.20 mm. The core wire have a radius of 2.58 mm, whereas the helical wire have a radius of 2.50 mm. Additionally, to estimate the deepest pit and calculate the loss of the cross-sectional area, a pit gauge was employed to measure the depth of the pits in each helical wire, as shown in Fig. 12(b) (ASTM G49-94, 2005). It was assumed that the core wire, which is not amenable to visual inspection, remained uncorroded (Jeon et al., 2019, 2023).

Table 3
Summary of prediction results based on simulated corrosion scenarios indicating number and percentage of specimens within probabilistic prediction bounds.

Mechanical properties	Within 50 % prediction bounds	Within 95 % prediction bounds	Within 99 % prediction bounds
F_u	507 (50.70 %)	954 (95.40 %)	988 (98.80 %)
F_y	508 (50.80 %)	946 (94.60 %)	992 (99.20 %)
F_u/F_y	578 (57.80 %)	960 (96.00 %)	993 (99.30 %)
D_u	478 (47.80 %)	938 (93.80 %)	990 (99.00 %)
D_y	505 (50.50 %)	934 (93.40 %)	986 (98.60 %)
D_u/D_y	572 (57.20 %)	962 (96.20 %)	994 (99.40 %)

After the pit depth was measured, tensile tests were performed on the specimens using the experimental setup shown in Fig. 12(c). A universal testing machine subjected the specimens to a displacement-controlled method and loaded these at a constant rate of 5 mm/min until failure occurred in the wire. Table 4 presents the results of the tensile tests, including the ultimate strength, ultimate displacement, yield strength, yield displacement, strength ratio, ductility ratio, number of corroded wires, and ratio of the corroded to nominal wire cross-sectional areas. For a strand with multiple corroded wires (such as Specimen 7, which has three corroded wires), η_w is denoted with slashes, e.g., 6.94/0.68/1.42. More detailed information on the test specimens was presented in previous studies (Lee et al., 2020; Jeon et al., 2023).

4.2. Uncertainties of corroded strand specimens

In this study, additional uncertainty factors were considered for the corroded strand specimens, unlike the previously discussed scenario-based corrosion. These sources of uncertainty are categorized into two types: (1) uncertainty in the material properties and (2) uncertainty in the geometric complexity of the corroded strand. First, as mentioned previously, the uncertainty in material property pertains to the Ramberg–Osgood curve parameters used in the FE simulations. The RVs considered included the ultimate strength, ultimate strain, elastic modulus, and yield strength of the steel wire. Their statistical properties are detailed in Table 1. Meanwhile, the geometric uncertainties include the variations in steel wire diameters, α of helical wires, and section loss estimation error (λ) due to idealized pit configurations. According to the International Organization for Standardization (ISO) tolerance levels for steel wire diameters (ISO 16124, 2004), Lee et al. (2020) identified inherent uncertainties in the diameters of steel wires and considered both core (d_c) and helical wire diameters (d_h) as RVs (Lee et al., 2020). The α influences the performance by affecting the load distribution among the wires, thereby affecting both strength and flexibility (Ghoreishi et al., 2007; Foti and Di Roseto, 2016). For example, a smaller α makes a strand stronger but less flexible, whereas a larger angle provides a higher flexibility but reduces the strength.

To account for this, the α of 125 stranded specimens were measured. The probability distribution is shown in Fig. 13(a) as a frequency histogram. The distribution was assessed using the Kolmogorov–Smirnov (K–S) test (Ang and Tang, 2007), which validated that the α follows a log-normal distribution. Based on these results, we employed a parametric probability distribution framework using MATLAB's *fitdist* function to estimate the distribution parameters including the mean and variance. Similarly, λ was quantified using the K–S test. Jeon et al. (2023) inspected 144 corroded steel wires to validate a corrosion assessment method based on pit depth measurements (Jeon et al., 2023). By comparing the section loss estimated by the pit depth method (denoted as A) with the area calculated using AutoCAD (denoted as B), the estimation error ($\lambda = B/A$) was determined to be 0.82, with a standard deviation of 0.37. This error also follows a log-normal distribution, as shown in Fig. 13(b).

The estimation error was incorporated into the model by multiplying it by the section loss. This approach is designed to mitigate discrepancies arising from the use of idealized pit geometries in representing real-world corrosion scenarios. While simplified pit shapes are employed in the FE model for computational feasibility and model generalization, λ bridges the gap between these idealized representations and the complex corrosion morphologies observed in practice. Specifically, this RV quantifies discrepancies between the model's geometric assumptions and actual section loss, improving predictive accuracy by accounting for the inherent variability of real-world corrosion. The statistical properties of RVs representing geometric complexity are detailed in Table 5. The RVs presented in Tables 1 and 5 correspond to the specific steel strand specimens analyzed in this study.

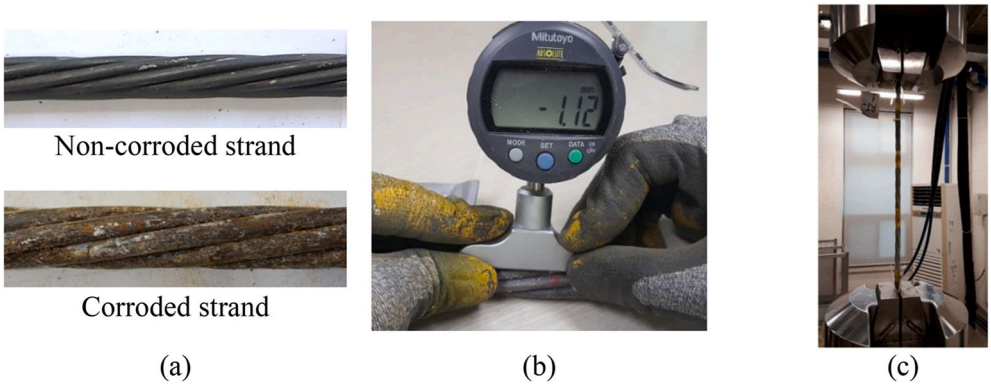

Fig. 12. (a) Test strand specimens; (b) Measuring pit depth using a pit depth gauge; (c) tensile test setup.

Table 4
Summary of tensile test results for strand specimens.

Specimen ID	F_u [kN]	D_u [mm]	F_y [kN]	D_y [mm]	F_u/F_y	D_u/D_y	N_{cw}	η_w (%)	Ref.
1	262.10	39.73	213.66	10.75	1.23	3.70	1	3.87	Jeon et al. (2023)
2	230.08	10.92	204.96	7.55	1.12	1.45	1	10.09	
3	246.38	26.16	202.52	7.52	1.22	3.48	2	5.50/0.92	
4	257.75	49.96	216.28	8.65	1.19	5.78	1	3.07	
5	230.56	10.61	207.45	7.82	1.11	1.36	3	7.62/6.34/0.60	
6	251.46	37.13	215.77	8.85	1.17	4.19	1	3.45	
7	221.62	10.03	201.32	7.58	1.10	1.32	3	6.94/0.68/1.42	
8	240.01	18.58	218.13	8.89	1.10	2.09	3	6.13/2.18/12.22	
9	257.74	29.95	219.99	9.36	1.17	3.20	1	8.03	
10	255.54	46.19	207.96	7.67	1.23	6.02	1	5.03	
11	256.89	39.98	207.21	7.55	1.24	5.30	2	2.08/5.74	
12	256.34	51.60	210.40	7.89	1.22	6.54	1	2.19	
13	260.48	48.61	223.14	9.45	1.17	5.14	2	1.25/1.25	
14	258.93	52.43	209.03	8.05	1.24	6.52	1	1.03	
15	251.88	34.16	212.25	8.21	1.19	4.16	3	10.68/8.31/6.28	
16	250.22	39.15	205.53	8.20	1.22	4.78	2	9.17/4.56	
17	264.65	57.49	220.71	8.72	1.20	6.59	–	–	
18	260.42	55.65	211.78	8.13	1.23	6.84	–	–	
19	255.13	43.51	206.73	7.66	1.23	5.68	1	2.66	
20	263.09	49.33	213.79	8.01	1.23	6.16	2	1.39/1.08	
21	264.47	53.21	214.58	7.98	1.23	6.67	1	3.17	
22	260.55	52.81	215.03	8.32	1.21	6.35	1	6.12	
23	256.76	37.55	212.05	8.25	1.21	4.55	3	4.64/2.18/1.08	
24	226.28	9.63	206.75	7.94	1.09	1.21	2	10.08/21.09	
25	258.70	41.07	212.79	8.01	1.22	5.13	1	7.06	
26	229.39	8.05	212.68	6.44	1.08	1.25	5	10.41/10.41/10.15/4.05/3.29	
27	240.16	13.69	213.78	6.63	1.12	2.06	5	13.45/9.64/3.29/1.76/1.50	
28	228.33	8.17	214.08	6.73	1.07	1.21	3	8.49/3.32/1.50	
29	227.52	8.27	213.74	6.86	1.06	1.21	4	10.66/7.61/4.29/0.74	
30	227.99	7.81	214.89	6.58	1.06	1.19	2	3.54/10.41	
31	254.40	23.48	211.16	6.23	1.20	3.77	4	7.36/2.01/5.32/2.01	
32	216.14	8.02	201.10	6.47	1.07	1.24	5	23.02/3.72/2.78/0.45/6.45	
33	235.21	10.33	207.23	6.39	1.14	1.62	5	6.85/0.74/7.61/19.26/9.14	
34	265.97	36.93	221.07	6.32	1.20	5.84	2	3.54/6.85	
35	234.41	12.52	211.48	8.45	1.11	1.48	2	20.28/6.87	Lee et al. (2020)
36	239.07	20.13	203.25	7.60	1.18	2.65	1	6.42	
37	255.13	43.51	206.73	7.66	1.23	5.68	1	2.68	
38	263.44	52.55	221.97	8.07	1.19	6.52	3	0.76/2.04/2.80	
39	231.50	10.30	217.37	8.50	1.06	1.21	3	17.9/1.84/3.20	

4.3. Analysis results

Using the proposed method, we probabilistically predicted the mechanical behavior of 39 steel strands. For each strand specimen, 10,000 random samples were generated using MCS. The statistical characteristics of the RVs were incorporated, as listed in Tables 1 and 5 The prediction outcomes are provided in Fig. 14(a)–(c). It shows three selected strands with varying degrees of corrosion: non-corroded (specimen 18), moderately corroded (specimen 3), and severely corroded (specimen 24). Comprehensive results for all the tested specimens are presented in Appendix A. In Fig. 14, the probabilistic predictions are compared with the tensile test results, as indicated by the red dotted lines. As illustrated, the failure points for each specimen were within the predicted ranges. The predicted mechanical behavior corresponded well with the experimental outcomes.

Fig. 15 presents a comprehensive analysis of the mechanical properties. It shows the varying uncertainty bounds depending on the specific properties. For example, the ultimate strength of specimen 24 (severely corroded) exhibited the widest uncertainty bounds. It was characterized by a coefficient of variation (COV) of 7.11 %. In contrast, the ultimate displacement of specimen 3 (moderately corroded) exhibited the broadest uncertainty range. It had a COV of 27.93 %. These differences may have originated from factors such as the variability in the corrosion morphology, geometric complexities, irregular

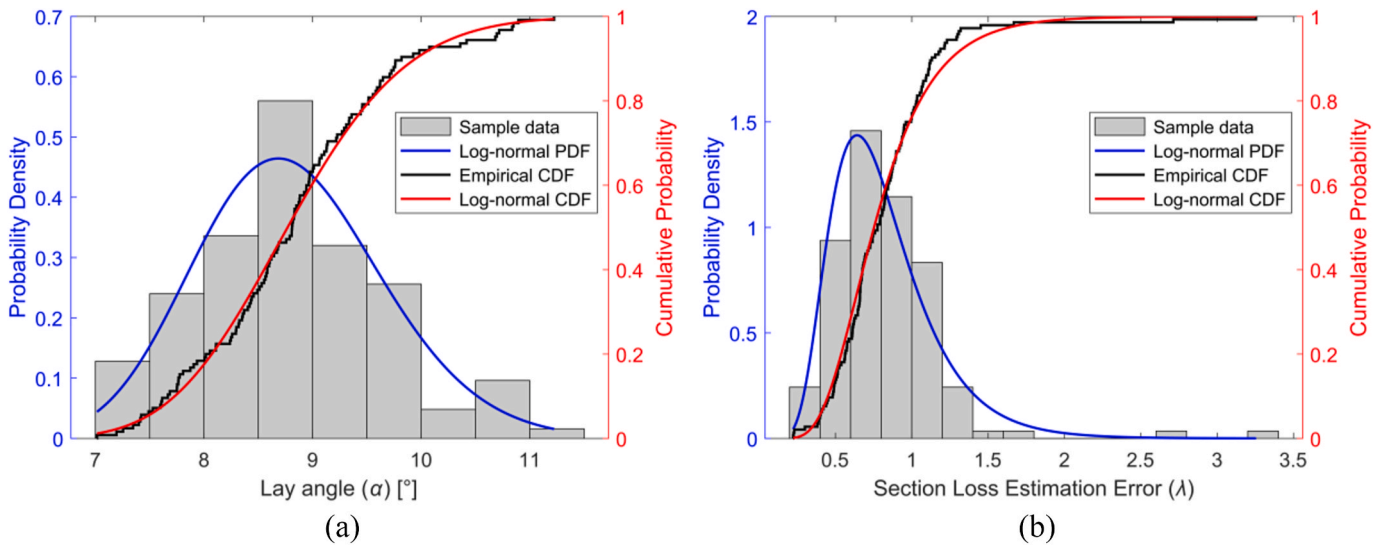

Fig. 13. K–S goodness-of-fit test of probability distributions for: (a) lay angle and (b) section loss estimation error.

Table 5
Statistical properties of RVs in geometric complexity.

RV	Mean	Coefficient of variation	Distribution type	Correlation coefficient			
				d_c	d_h	α	λ
d_c	5.16 mm	0.012	Normal	1.0			Sym.
d_h	5.00 mm	0.012	Normal	0	1.0		
α	8.81°	0.100	Log-normal	0	0	1.0	
λ	0.82	0.450	Log-normal	0	0	0	1.0

interactions between wires, and potential measurement errors in the pit depth and cross-sectional area assessments. These factors introduce additional unpredictability into the strand responses. This contributes to the observed uncertainty in the strength and displacement predictions for the given corrosion states. This finding contrasts with the scenario-based predictions, where severe corrosion typically results in narrower uncertainty ranges. Therefore, the results emphasize the necessity of accurately quantifying and incorporating additional uncertainty factors in real strand specimens. By including these factors, the prediction model could capture the variability in the mechanical behavior across various stages of corrosion more effectively.

In Appendices A and B and, the probabilistic prediction results for the 39 specimens are presented (see Figs. 14 and 15). Table 6 summarizes the performance of the proposed method in predicting the six mechanical properties of the 39 specimens based on a quantitative analysis similar to that shown in Table 3. The method exhibited reasonable predictive accuracy: the yield strength was fully captured within the 95 % and 99 % prediction bounds for all the 39 specimens (100 %). Additionally, the ultimate strength was predicted for 38 out of 39 specimens (97.44 %) within the 99 % bounds, whereas the ultimate displacement and yield displacement predictions fell within the 99 % bounds for 36 (92.31 %) and 35 (89.74 %) specimens, respectively. The prediction accuracies for the strength and ductility ratios were 94.87 % and 87.18 %, respectively.

5. Conclusion

This study developed a probabilistic framework for predicting the non-linear mechanical behavior of corroded steel strands, addressing the need for a reliable assessment of deteriorating PSC structures. The methodology integrates 3D FE modeling, a GPR-based multi-surrogate model, and probabilistic analysis using MCS and KDE, enabling load–displacement prediction while incorporating uncertainty.

A key finding is that this approach not only predicts the structural behavior of corroded strands but also quantifies associated uncertainties, allowing for a more comprehensive evaluation of corrosion effects compared to deterministic models. By incorporating eight RVs representing geometric and material uncertainties, the method

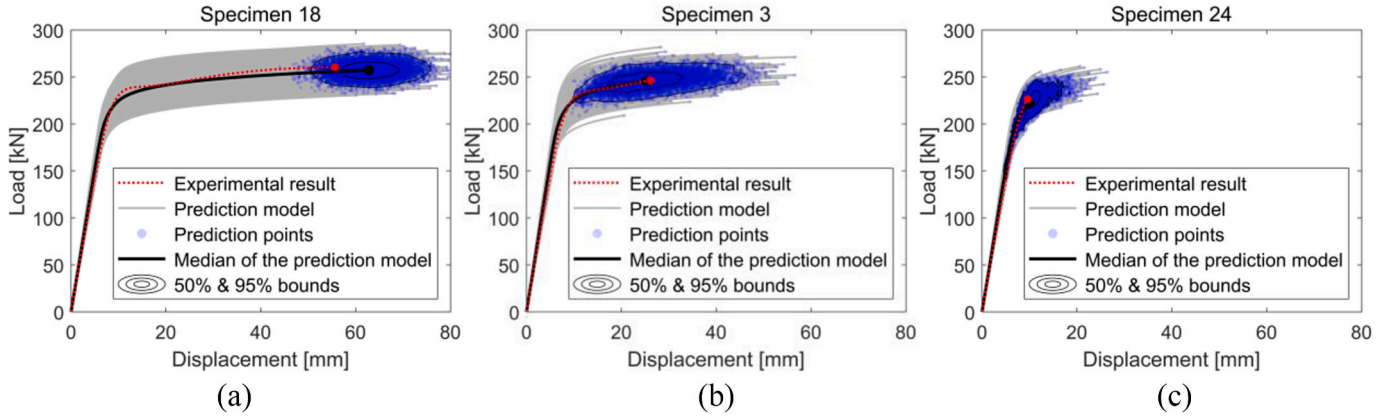

Fig. 14. Probabilistic prediction results of load–displacement curves for selected test specimens: (a) non-corroded strand (specimen 18); (b) moderately corroded strand (specimen 3); and (c) severely corroded strand (specimen 24).

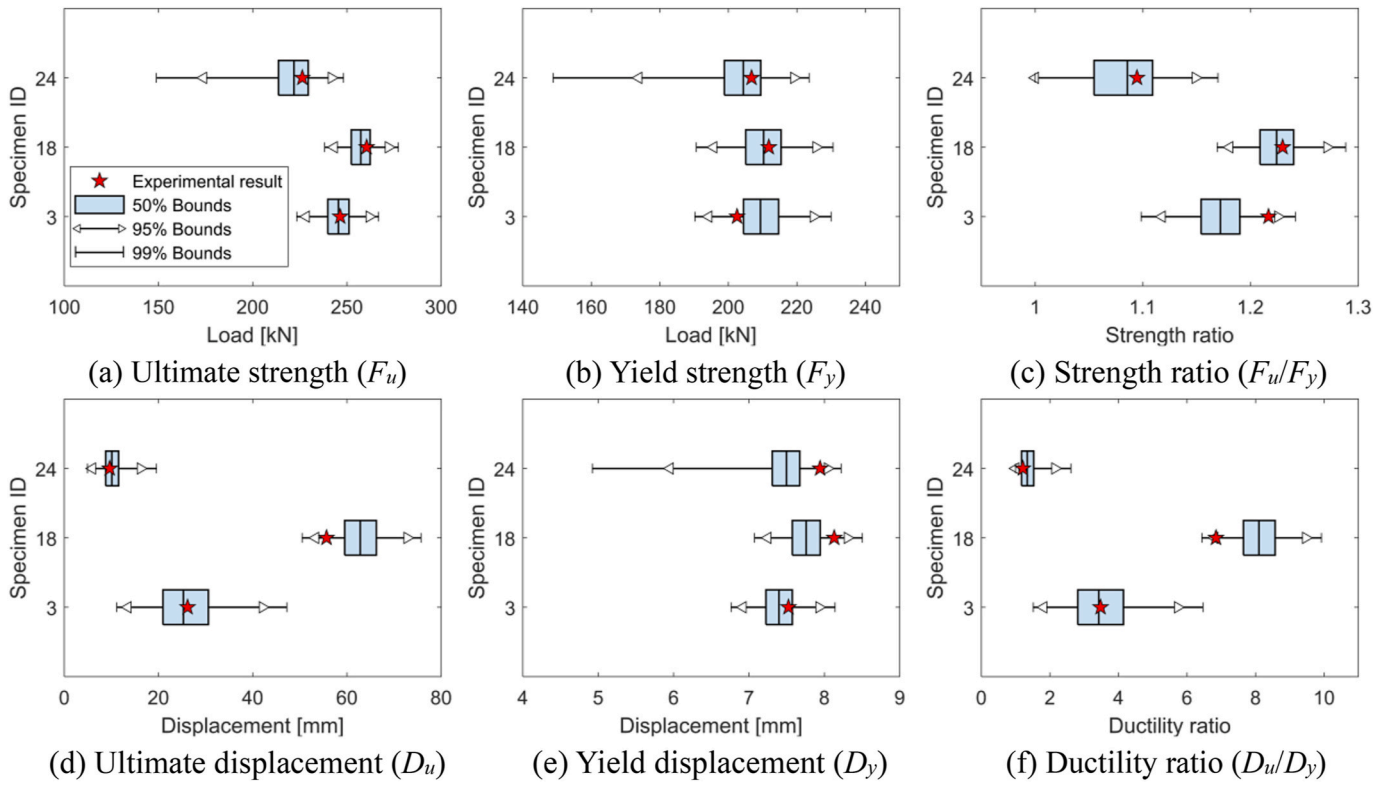

Fig. 15. Probabilistic prediction bounds compared with experimental results for the mechanical properties of selected test specimens.

Table 6
Summary of prediction results indicating number and percentage of specimens within probabilistic prediction ranges based on experimental results.

Mechanical properties	Within 50 % prediction bounds	Within 95 % prediction bounds	Within 99 % prediction bounds
F_u	13 (33.33 %)	37 (92.31 %)	38 (97.44 %)
F_y	19 (48.72 %)	39 (100.00 %)	39 (100.00 %)
F_u/F_y	12 (30.77 %)	32 (82.05 %)	37 (94.87 %)
D_u	11 (28.21 %)	27 (69.23 %)	36 (92.31 %)
D_y	15 (38.46 %)	32 (82.05 %)	35 (89.74 %)
D_u/D_y	12 (30.77 %)	27 (69.23 %)	34 (87.18 %)

effectively captures variability across different corrosion conditions, ensuring robust performance across diverse scenarios. Validation with 39 corroded strand specimens from in-service PSC box bridges demonstrated high predictive accuracy, particularly for ultimate and yield strength, with 97.44 % of ultimate strength values falling within the 99 % prediction bounds.

While the results demonstrate the effectiveness of the proposed framework, several aspects could be further refined. Enhancing the FE model to better capture complex corrosion morphologies could improve predictive accuracy. Additionally, incorporating longitudinal corrosion variations and strand interactions, along with additional uncertainty factors, may improve the model's ability to represent real-world degradation more accurately. Expanding validation with larger datasets and diverse strand types would further strengthen its applicability to practical engineering assessments.

The proposed method is expected to contribute to more reliable assessments of corroded PSC structures by enabling probabilistic evaluations of PSC girders and bridges. While further refinement is needed, this framework offers valuable insights that can support improved infrastructure management and durability assessments.

CRediT authorship contribution statement

Seungjun Lee: Writing – original draft, Visualization, Validation, Methodology, Investigation, Formal analysis, Conceptualization. **Jaebeom Lee:** Writing – review & editing, Supervision, Funding acquisition, Conceptualization. **Chi-Ho Jeon:** Writing – review & editing, Data curation. **Young-Joo Lee:** Writing – review & editing, Supervision, Funding acquisition, Conceptualization.

Declaration of competing interest

The authors declare that they have no known competing financial interests or personal relationships that could have appeared to influence the work reported in this paper.

Acknowledgements

This work was supported by the National Research Foundation of Korea (NRF) grant funded by the Korea government (MSIT) (2021R1C1C2008770). This work was also supported by the National Research Foundation of Korea (NRF) grant funded by the Korea government (MSIT) (No. RS-2022-00144434).

Appendix A. Probabilistic prediction and experimental results for test specimens 1–39

The probabilistic predictions and experimental results for the test specimens are shown in Fig. A. 1.

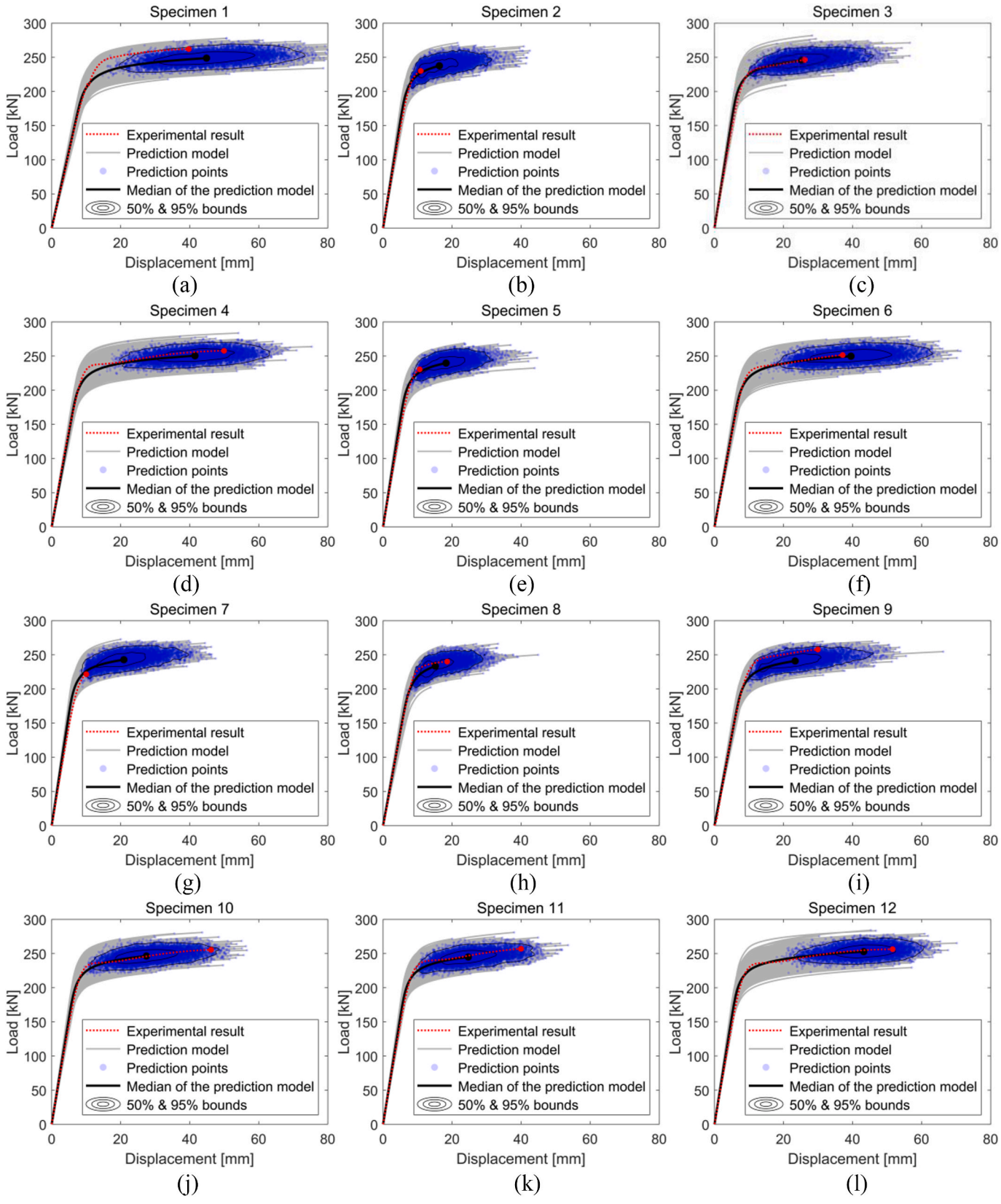

Fig. A. 1. Probabilistic prediction results of load–displacement curve of 39 specimens.

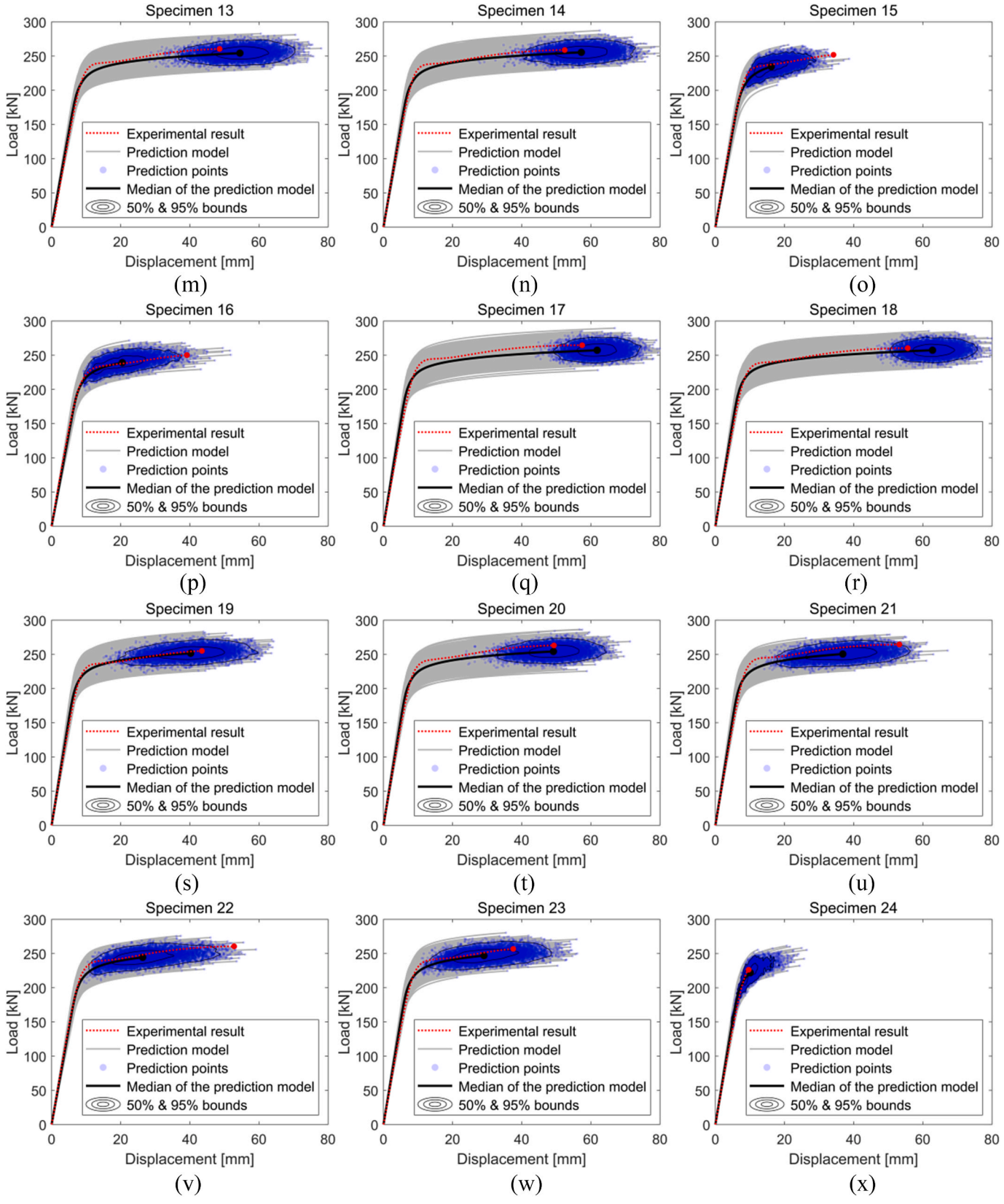

Fig. A. 1. (*continued*).

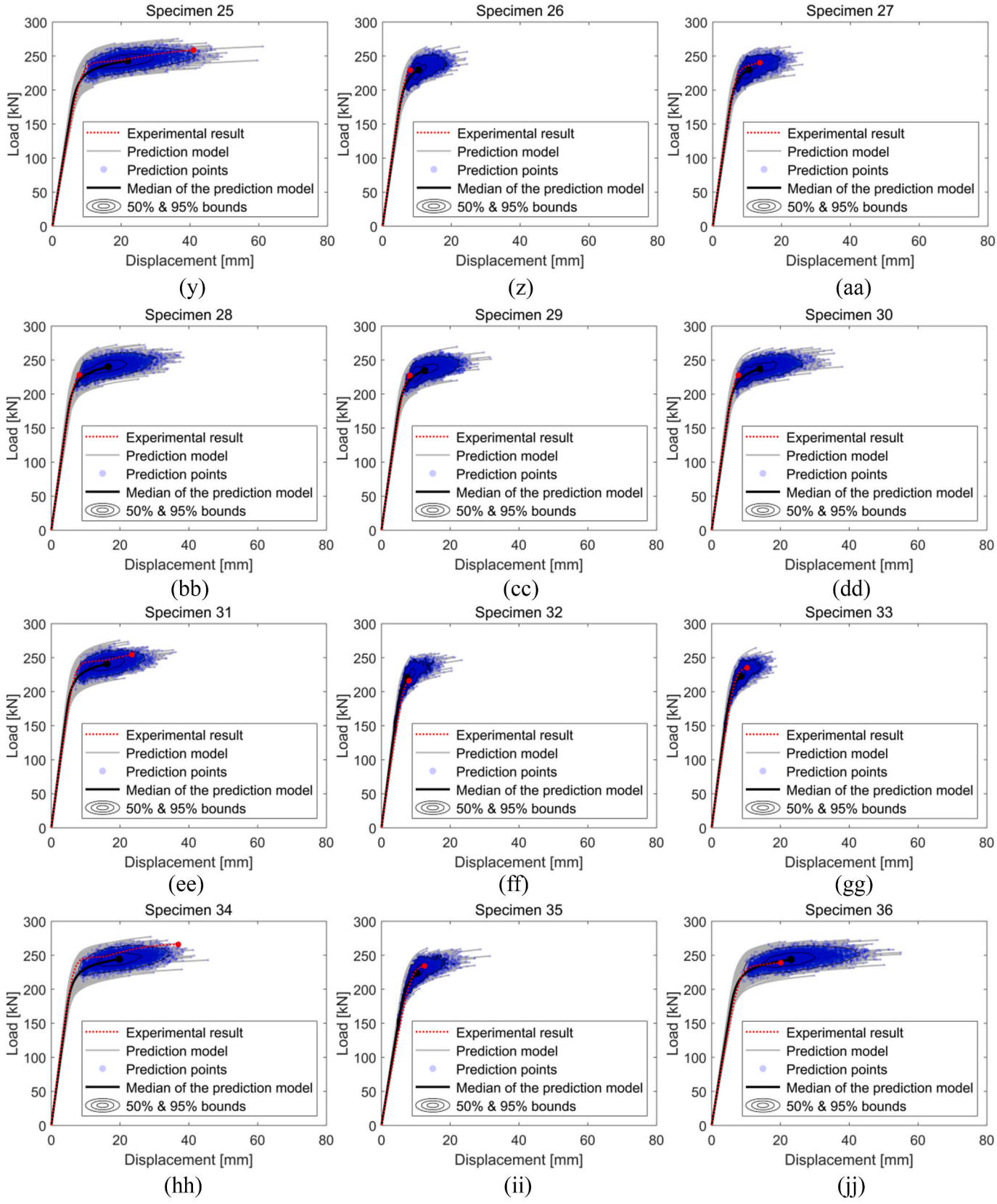

Fig. A. 1. (*continued*).

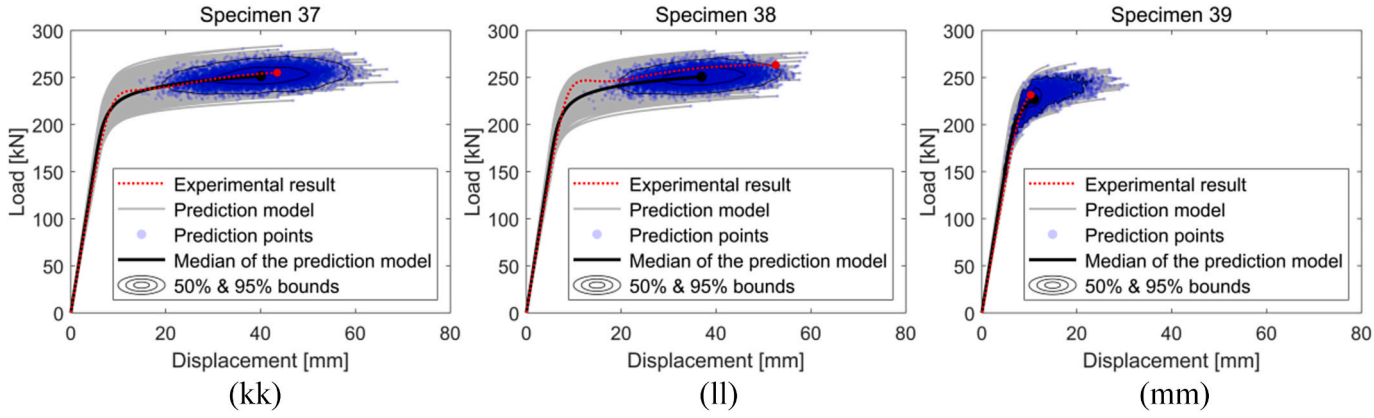

Fig. A. 1. (*continued*).

Appendix B. Probabilistic prediction bounds compared with experimental results for mechanical properties of test specimens 1–39

The probabilistic prediction bounds compared with the experimental results for the mechanical properties of the specimens are shown in Fig. B. 1.

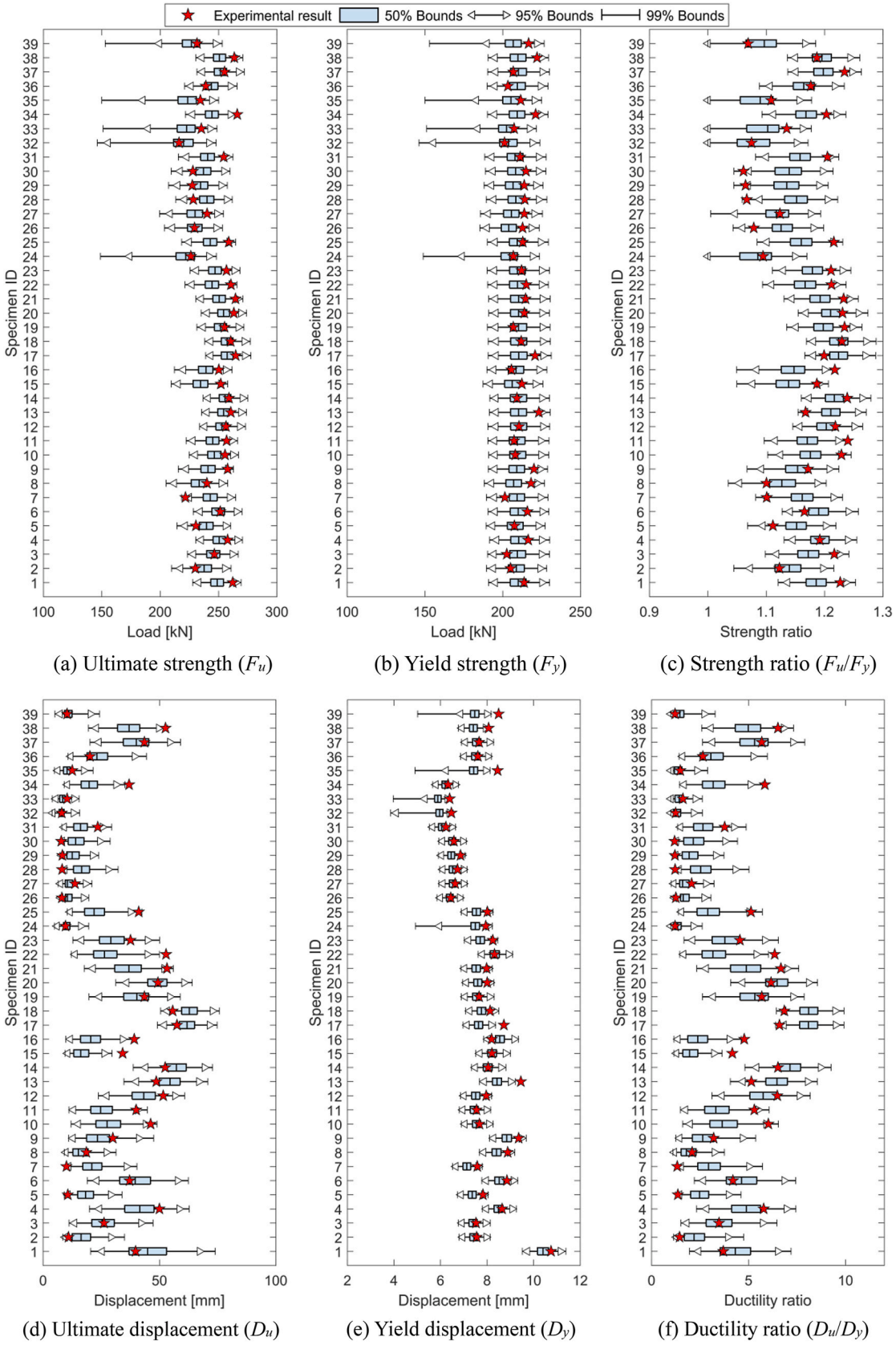

Fig. B. 1. Probabilistic prediction bounds compared with experimental results for the mechanical properties of 39 specimens.

Data availability

Data will be made available on request.

References

Abdullah, A.B.M., Rice, J.A., Hamilton, H.R., Consolazio, G.R., 2016. An investigation on stressing and breakage response of a prestressing strand using an efficient finite element model. Eng. Struct. 123, 213–224. https://doi.org/10.1016/j.engstruct.2016.05.030.

Ang, A.H.-S., Tang, W.H., 2007. Probability Concepts in Engineering: Emphasis on Applications to Civil and Environmental Engineering, second ed. John Wiley & Sons.

ASTM G49-94, 2005. Standard Guide for Examination and Evaluation of Pitting Corrosion. ASTM International, West Conshohocken, PA.

Biondini, F., Frangopol, D.M., 2018. Life-cycle performance of civil structure and infrastructure systems: survey. J. Struct. Eng. 144, 06017008. https://doi.org/10.1061/(ASCE)ST.1943-541X.0001923.

Chen, Y., Qin, W., Wang, Q., Tan, H., 2021. Influence of corrosion pit on the tensile mechanical properties of a multi-layered wire rope strand. Constr. Build. Mater. 302, 124387. https://doi.org/10.1016/j.conbuildmat.2021.124387.

Costello, G.A., 1997. Theory of Wire Rope. Springer Science & Business Media.

Darmawan, M.S., Stewart, M.G., 2007. Effect of pitting corrosion on capacity of prestressing wires. Mag. Concr. Res. 59, 131–139. https://doi.org/10.1680/macr.2007.59.2.131.

De Schutter, G., 2013. Damage to Concrete Structures. CRC Press, Taylor & Francis Group, pp. 31–33.

EN 10138-3, Prestressing Steels – Part 3: Strand, 2009. European Committee for Standardization (CEN), Brussels, Belgium.

Foti, F., Di Roseto, A.D.L., 2016. Analytical and finite element modelling of the elastic–plastic behaviour of metallic strands under axial–torsional loads. Int. J. Mech. Sci. 115, 202–214. https://doi.org/10.1016/j.ijmecsci.2016.06.016.

Franceschini, L., Vecchi, F., Tondolo, F., Belletti, B., Montero, J.S., 2022. Mechanical behaviour of corroded strands under chloride attack: a new constitutive law. Constr. Build. Mater. 316, 125872. https://doi.org/10.1016/j.conbuildmat.2021.125872.

Ghoreishi, S.R., Messager, T., Cartraud, P., Davies, P., 2007. Validity and limitations of linear analytical models for steel wire strands under axial loading, using a 3D FE model. Int. J. Mech. Sci. 49, 1251–1261. https://doi.org/10.1016/j.ijmecsci.2007.03.014.

Gnanavel, B.K., Parthasarathy, N.S., 2012. Effect of interfacial contact forces in single layer cable assemblies. Int. J. Mech. Mater. Des. 8, 183–195. https://doi.org/10.1007/s10999-012-9185-7.

ISO 16124, 2004. Steel Wire Rod — Dimensions and Tolerances. International Organization for Standardization (ISO), Switzerland.

Jacinto, L., Pipa, M., Neves, L.A., Santos, L.O., 2012. Probabilistic models for mechanical properties of prestressing strands. Constr. Build. Mater. 36, 84–89. https://doi.org/10.1016/j.conbuildmat.2012.04.121.

JCSS, 2001. Probabilistic Model Code Part 3: Resistance Models. Joint Committee of Structural Safety (JCSS). Available from: https://www.jcss-lc.org/jcss-probabilistic-model-code/ (Accessed 1 September 2024).

Jeon, C.-H., Lee, J.-B., Lon, S., Shim, C.-S., 2019. Equivalent material model of corroded prestressing steel strand. J. Mater. Res. Technol. 8, 2450–2460. https://doi.org/10.1016/j.jmrt.2019.02.010.

Jeon, C.-H., Nguyen, C.D., Shim, C.-S., 2020. Assessment of mechanical properties of corroded prestressing strands. Appl. Sci. 10, 4055. https://doi.org/10.3390/app10124055.

Jeon, C.-H., Oeurn, S., Shim, C.-S., 2023. Test database for corroded prestressing steel strands recovered from aged bridges. J. Mater. Civ. Eng. 35, 05022003. https://doi.org/10.1061/(ASCE)MT.1943-5533.0004557.

Judge, R., Yang, Z., Jones, S.W., Beattie, G., 2012. Full 3D finite element modelling of spiral strand cables. Constr. Build. Mater. 35, 452–459. https://doi.org/10.1016/j.conbuildmat.2011.12.073.

Lee, S.K., 2022. Corrosion-induced durability issues and maintenance strategies for post-tensioned concrete bridges. Federal Highway Administration, Office of Infrastructure Research and Development. https://doi.org/10.21949/1521873 (No. FHWA-HRT-22-090).

Lee, J., Lee, Y.-J., Shim, C.-S., 2020. Probabilistic prediction of mechanical characteristics of corroded strands. Eng. Struct. 203, 109882. https://doi.org/10.1016/j.engstruct.2019.109882.

Li, R., Miao, C., Yu, J., 2020. Effect of characteristic parameters of pitting on strength and stress concentration factor of cable steel wire. Constr. Build. Mater. 240, 117915. https://doi.org/10.1016/j.conbuildmat.2019.117915.

Liu, X., Zhang, W., Gu, X., Zeng, Y., 2017. Degradation of mechanical behavior of corroded prestressing wires subjected to high-cycle fatigue loading. J. Bridge Eng. 22 (5), 04017004. https://doi.org/10.1061/(ASCE)BE.1943-5592.0001025.

Liu, X., Zhang, W., Gu, X., Ye, Z., 2021. Probability distribution model of stress impact factor for corrosion pits of high-strength prestressing wires. Eng. Struct. 230, 111686. https://doi.org/10.1016/j.engstruct.2020.111686.

Lu, Z., Li, F., Zhao, Y.G., 2016. An investigation of degradation of mechanical behaviour of prestressing strands subjected to chloride attacking. In: Proc. 5th Int. Conf. Durab. Concr. Struct. Shenzhen University, Shenzhen, Guangdong Province, China, pp. 57–65. https://doi.org/10.5703/1288284316111.

McKay, M.D., Beckman, R.J., Conover, W.J., 1979. Comparison of three methods for selecting values of input variables in the analysis of output from a computer code. Technometrics 21, 239–245. https://doi.org/10.1080/00401706.1979.10489755.

Parzen, E., 1962. On estimation of a probability density function and mode. Ann. Math. Stat. 33, 1065–1076. https://doi.org/10.1214/aoms/1177704472.

Ramberg, W., Osgood, W.R., 1943. Description of Stress-Strain Curves by Three Parameters. National Advisory Committee for Aeronautics (No. NACA-TN-902).

Rasmussen, C.E., Nickisch, H., 2015. Gaussian processes for machine learning (GPML) toolbox. J. Mach. Learn. Res. 11, 3011–3015. https://doi.org/10.5555/1756006.1953029.

Rasmussen, C.E., Williams, C.K.I., 2005. Gaussian Processes for Machine Learning. The MIT Press.

Rosenblatt, M., 1956. Remarks on some nonparametric estimates of a density function. Ann. Math. Stat. 27, 832–837. https://doi.org/10.1214/aoms/1177728190.

Silverman, B.W., 2018. Density Estimation for Statistics and Data Analysis. Routledge.

Spak, K., Agnes, G., Inman, D., 2013. Cable modeling and internal damping developments. Appl. Mech. Rev. 65, 010801. https://doi.org/10.1115/1.4023489.

Systèmes, Dassault, 2016. ABAQUS Version 2016 Documentation. Dassault Systèmes, Simulia Corp., Providence, RI.

Viana, F.A., 2016. A tutorial on Latin hypercube design of experiments. Qual. Reliab. Eng. Int. 32, 1975–1985. https://doi.org/10.1002/qre.1924.

Vu, N.A., Castel, A., François, R., 2009. Effect of stress corrosion cracking on stress–strain response of steel wires used in prestressed concrete beams. Corros. Sci. 51, 1453–1459. https://doi.org/10.1016/j.corsci.2009.03.033.

Wang, L., Li, T., Dai, L., Chen, W., Huang, K., 2020. Corrosion morphology and mechanical behavior of corroded prestressing strands. J. Adv. Concr. Technol. 18, 545–557. https://doi.org/10.3151/jact.18.545.

Woodward, R.J., Williams, F.W., 1988. Collapse of yns-Y-gwas bridge, glamorgan. Proc. Inst. Civ. Eng. 84, 635–669. https://doi.org/10.1680/iicep.1988.179.

Yu, Y., Chen, Z., Liu, H., Wang, X., 2014. Finite element study of behavior and interface force conditions of seven-wire strand under axial and lateral loading. Constr. Build. Mater. 66, 10–18. https://doi.org/10.1016/j.conbuildmat.2014.05.009.

Zhang, X., Wang, L., Zhang, J., Liu, Y., 2017. Corrosion-induced flexural behavior degradation of locally ungrouted post-tensioned concrete beams. Constr. Build. Mater. 134, 7–17. https://doi.org/10.1016/j.conbuildmat.2016.12.140.

Zhang, W.P., Li, C.K., Gu, X.L., Zeng, Y.H., 2019. Variability in cross-sectional areas and tensile properties of corroded prestressing wires. Constr. Build. Mater. 228, 116830. https://doi.org/10.1016/j.conbuildmat.2019.116830.